J. Fluid Mech. (2012), *vol.* 690, *pp.* 399–425.
doi:10.1017/jfm.2011.445

Eigenmodes of lined flow ducts with rigid splices

E.J. BRAMBLEY[1]†, A.M.J. DAVIS[2] AND N. PEAKE[1]

[1]Department of Applied Mathematics and Theoretical Physics, University of Cambridge, Wilberforce Road, Cambridge, CB3 0WA, UK

[2]Department of Mechanical and Aerospace Engineering, University of California San Diego, 9500 Gilman Drive, La Jolla, CA 92093-0411, USA

(Received Received 28 April 2011; revised 11 August 2011; accepted 6 October 2011; first published online 28 November 2011)

This paper presents an analytic expression for the acoustic eigenmodes of a cylindrical lined duct with rigid axially running splices in the presence of flow. The cylindrical duct is considered to be uniformly lined except for two symmetrically positioned axially running rigid liner splices. An exact analytic expression for the acoustic pressure eigenmodes is given in terms of an azimuthal Fourier sum, with the Fourier coefficients given by a recurrence relation. Since this expression is derived using a Green's function method, the completeness of the expansion is guaranteed. A numerical procedure is described for solving this recurrence relation, which is found to converge exponentially with respect to number of Fourier terms used and is in practice quick to compute; this is then used to give several numerical examples for both uniform and sheared mean flow. An asymptotic expression is derived to directly calculate the pressure eigenmodes for thin splices. This asymptotic expression is shown to be quantitatively accurate for ducts with very thin splices of less than 1% unlined area and qualitatively helpful for thicker splices of the order of 6% unlined area. A thin splice is in some cases shown to increase the damping of certain acoustic modes. The influences of thin splices and thin boundary layers are compared and found to be of comparable magnitude for the parameters considered. Trapped modes at the splices are also identified and investigated.

Key words: aeroacoustics, shear layers, wave-structure interactions

1. Introduction

Turbofan aeroengines are routinely fitted with acoustic linings in the intake and bypass ducts to reduce noise. Owing to construction constraints, these liners have traditionally been manufactured in two semicircular pieces which are then joined together, leaving a thin unlined strip along the join, termed a *splice*. The effect of even thin liner splices has long been thought to be significant, although earlier studies (see, for example, Fuller 1984, and references therein) were limited by the computational resources available at the time. For example, Fuller restricted himself to no flow, a half-lined half-unlined duct and a maximum Helmholtz number of 10, in order to reduce the computational complexity.

The importance of splices was demonstrated experimentally by Sarin & Rademaker

† Email address for correspondence: E.J.Brambley@damtp.cam.ac.uk

(1993), who made in-flight measurements on a Rolls–Royce Tay 650 turbofan engine fitted to a Fokker 100 aeroplane, backed up by laboratory experiments (Rademaker, Sarin & Parente 1996). Modern attempts to theoretically model the effect of liner splices for realistic parameters could be said to begin with Regan & Eaton (1999), who considered an infinite rigid cylindrical duct containing a uniform mean flow and fitted with a finite-length lined section with two thin rigid splices. Regan & Eaton investigated this situation numerically using a three-dimensional finite-element computation, and concluded that liner splices can significantly influence the transmitted acoustic field and that further investigation was needed. Other numerical investigations of the same geometry have been performed by Duta & Giles (2006) using Fourier modes azimuthally coupled with two-dimensional finite elements, and McAlpine & Wright (2006), who used three-dimensional finite elements for reduced *model scale* parameters and found that scattering by liner splices can adversely affect fan tone noise levels at lower supersonic fan speeds (a 13dB reduction in attenuation was predicted) but have little adverse affect on noise levels at higher supersonic fan speeds typical of takeoff. A completely different type of numerical calculation using the boundary integral method and mode-matching has been performed by Yang & Wang (2008) for a finite-length lined section within either a finite or infinite rigid duct with uniform mean flow, including the propagation to the far field from a finite-length duct, who find the presence of splices slightly increases the maximum sound pressure level while the angle of the maximum sound pressure level remains approximately the same. While all of these studies have been completed in the frequency domain, Tam, Ju & Chien (2008) completed numerical time-domain simulations, again assuming uniform flow. They used this time-domain simulation to perform several parametric studies of upstream-propagating sound, concluding that splices had little effect for widths of 1/100th of a duct radius or smaller, and that the primary effect of the splices was for the downstream liner edge to scatter the incoming sound with equal energy into all cut-on duct modes.

Numerical investigations are also possible using the method developed by Watson (1981), by expanding the perturbation within the spliced section in terms of the eigenmodes of an unspliced duct, either lined or unlined; however, there is a question over the completeness of the expansion if lined duct modes are used, since the lined duct equation is not self-adjoint. A version of Watson's method, derived by Pagneux, Amir & Kergomard (1996) and termed the *multimodal method*, was used to investigate liner splices without flow by Bi *et al.* (2006, 2007). They found liner splices to have a negligible scattering effect for typical aeroacoustic parameters unless the output was dominated by an especially well attenuated mode, in which case they predicted liner splices could give a significant penalty, and they also found that when the phases of incident modes were incoherent the effect of the splices was reduced compared with when the phases of the incident modes were correlated. Subsequently, using the same multimodal method (again without flow), Bi *et al.* (2009) found trapped modes, which are eigenmodes of the lined spliced duct which are localized about the rigid liner splices.

Another approach is to consider the eigenmodes of the spliced lined duct, with the axial wavenumber forming the eigenvalue. Such an analysis was performed for an infinite lined duct by Fuller (1984) without flow and, more recently, by Campos & Oliveira (2004) including flow, although the boundary condition used by Campos & Oliveira is incorrect for nonzero mean flow (see Eversman & Beckemeyer 1972; Tester 1973). Both of these studies posed an expansion of the eigenfunction as a sum of solutions of the Helmholtz equation for the duct but, unlike the multimodal expansion of Pagneux *et al.* (1996), these solutions were not required to satisfy the boundary conditions but were required to all have the same axial wavenumber; a similar technique, although derived in a different

manner using a Green's function approach, is used here, and results in a singly infinite (Fourier) modal sum. In contrast, Bi (2008) tackled the eigenmode problem in an infinite spliced lined duct with uniform flow using a type of spectral method consisting of a modal decomposition in terms of hard-walled duct modes augmented by a pressure-release duct mode to aid faster convergence, leading to a doubly infinite modal sum. The spliced eigenmode problem has also been considered numerically by Wright (2006) and Gabard & Astley (2008), who both used two-dimensional finite elements to numerically calculate the eigenmodes within the lined section of a duct and then match these to the rigid-walled modes of the infinite rigid duct at either end of the lined section; both of these studies used a uniform mean flow. Gabard & Astley conclude that the influence of liner splices in the far-field is far from simple and that modal scattering at liner discontinuities can result in complex patterns of radiated noise.

Little real progress has been made by exploiting the thinness of the liner splices, as is generally the case in practice, with the only application of this assumption to date being faster numerical computation. Tester *et al.* (2006) presented a method due to Cargill (1993) based on the Kirchhoff approximation that the splices cause a small perturbation to the eigenmodes of a uniformly lined duct, which is effectively a small-scattering assumption. Tester & de Mercato (2006) extended this work to a finite-length duct including the propagation to the far field, and demonstrate for a realistic intake geometry the complex far-field directivity patterns that can be caused by liner splices. A variant of this method was given by Alonso & Burdisso (2007), who considered pistons placed along the splice (with two pistons per wavelength) driven so as to approximately satisfy the rigid wall boundary condition on the splice. An approximation for resolving thin splices in time-domain simulations without overly refining the computational mesh, effectively a sub-grid-scale model, was proposed by Tam & Ju (2009).

Although our method is readily generalized to any geometric configuration, in this paper we derive an expression for the duct pressure eigenmodes in an infinite lined duct with two rigid splices and arbitrary non-transonic axial mean flow. The eigenmodes of this duct are given in §3 in terms of a Fourier series, derived analytically without approximation using a Green's function method that is physically intuitive and leaves no question as to the azimuthal completeness of the expansion. The solution of the resulting recursion relation is given asymptotically for thin splices in §4 and numerically in §5. These are then used to give a number of example results in §6, including an investigation of the trapped modes found by Bi *et al.* (2009).

2. Problem Formulation

Consider the situation shown in figure 1 of a straight hollow cylindrical duct carrying an ideal fluid. The mean flow of the fluid is purely in the axial direction, with zero swirl, but with the axial speed varying with radius. We suppose that the mean density and mean pressure of the flow are uniform. In what follows, lengths are nondimensionalized using the duct radius d^*, densities using the mean density ρ^* and time using d^*/c_0^*, where c_0^* is the uniform sound speed. In this way the normalized axial mean flow speed is $M(r)$, the local Mach number (which is subsonic for the examples presented here), and r is the radial coordinate $0 \leqslant r \leqslant 1$.

We consider unsteady perturbations to this mean flow with fixed dimensionless frequency ω, the Helmholtz number for the cylinder, and fixed axial wavenumber k. In this way, the unsteady pressure perturbation can be written in the form $p(r,\theta)\exp\{\mathrm{i}kx-\mathrm{i}\omega t\}$, with r,θ,x the cylindrical polar coordinates for the duct and t the dimensionless time. We are interested in eigenmodes of the system in which the axial wavenumber k takes the

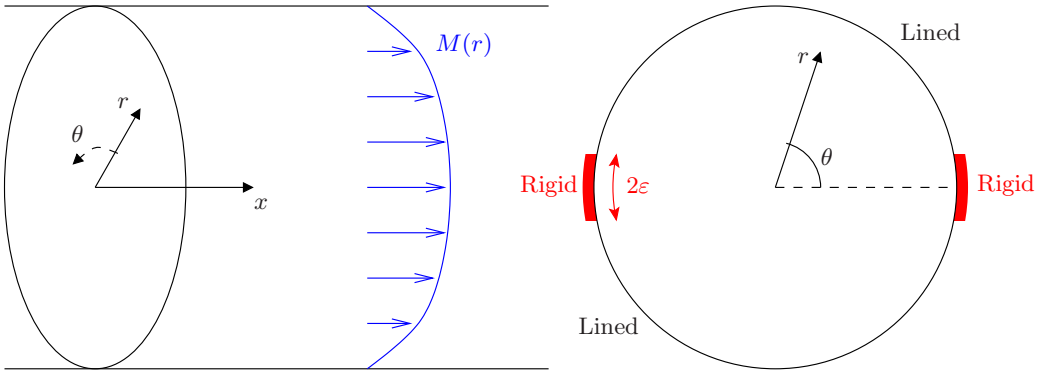

FIGURE 1. Geometry of a spliced duct with two symmetrically positioned rigid splices.

role of the eigenvalue. It should be noted that, for the general case of sheared axial mean flow, a continuous spectrum exists in addition to the discrete spectrum of eigenvalues k considered here (see, e.g. Swinbanks 1975), although this is not present in the special case of a uniform axial mean flow.

The equation satisfied by $p(r,\theta)$ is known as the Pridmore-Brown (1958) equation, as used by Vilenski & Rienstra (2007). Note that the Pridmore-Brown equation is generally written in the form applying to a single azimuthal wavenumber, so that $p(r,\theta) = p(r)\exp\{\mathrm{i}m\theta\}$, but it is a straightforward matter to derive this in the form suitable for the arbitrary θ dependence to give

$$\frac{1}{r}\frac{\partial}{\partial r}\left(r\frac{\partial p}{\partial r}\right)+\frac{1}{r^2}\frac{\partial^2 p}{\partial\theta^2}+\frac{2kM'}{\omega-Mk}\frac{\partial p}{\partial r}+\left[(\omega-Mk)^2-k^2\right]p=0\,. \tag{2.1}$$

Here a prime denotes differentiation of $M(r)$ with respect to radius. In the uniform-flow case $M'(r)=0$ and equation (2.1) reduces to the convected-Helmholtz equation for a uniform medium.

The wall of the cylinder is taken to be composed of a mixture of lined and rigid sections of infinite axial extent. In figure 1 we show the case considered in detail here, consisting of two large lined sections separated by two diametrically opposed rigid splices, although the theory presented here may be applied to arbitrary arrangements of lined and rigid sections. The lined sections are modelled as having a given complex impedance, Z, which is taken here to be uniform in θ and the same for each lined section. The boundary condition to be satisfied on the lined sections is the standard Myers condition (Eversman & Beckemeyer 1972; Tester 1973; Myers 1980),

$$\frac{\partial p}{\partial r}+\frac{(\omega-Mk)^2}{\mathrm{i}\omega Z}p=0 \quad \text{at } r=1 \text{ for } \theta\in L\,, \tag{2.2}$$

where L is the lined portion of the circumference. We note in passing that this boundary condition has recently proved contentious when used with slipping flow (Aurégan, Starobinski & Pagneux 2001; Brambley 2009, 2011*a*), and that any of the proposed modified boundary conditions (Aurégan *et al.* 2001; Joubert 2010; Rienstra & Darau 2011; Brambley 2011*b*) could be imposed instead; here, we retain the boundary condition as given in (2.2) for simplicity, while noting that this reduces to the uncontentious inviscid boundary condition for nonslipping mean flow, albeit with viscous effects important for low frequencies still neglected (Aurégan *et al.* 2001; Brambley 2011*a*). On the rigid

sections the boundary condition is

$$\frac{\partial p}{\partial r} = 0 \quad \text{at } r = 1 \text{ for } \theta \in R\,, \tag{2.3}$$

where R is the rigid portion of the circumference. Clearly $L \cup R$ is the whole circumference. We also require that $p(r,\theta)$ is regular at $r = 0$. From Osipov & Norris (1999, equations 109 and 111), we expect p to be continuous and $\partial p/\partial r$ to tend to zero near an edge between L and R. Our aim is to solve this system of equations to determine the spectrum of allowed values of k, and the corresponding mode shapes $p(r,\theta)$, for a given frequency ω.

3. The Green's function and integral equation formulation

In what follows we seek an integral equation depending only on the surface values $p(1,\theta)$, and to do this we need to calculate a specific Green's function $G(r,\theta;\theta_0)$. We suppose that $G(r,\theta;\theta_0)$ satisfies the governing equation (2.1), subject to the boundary condition

$$\frac{\partial G}{\partial r} + \frac{(\omega - Mk)^2}{\mathrm{i}\omega Z} G = \frac{(\omega - Mk)^2}{\mathrm{i}\omega Z}\delta(\theta - \theta_0) \qquad \text{on } \; r = 1 \tag{3.1}$$

for given θ_0. Note that (3.1) is the lined condition (2.2), except that we now include an impulse term on the right. This is precisely the form of Green's function used by Davis & Llewellyn Smith (2007), and earlier in a different context by LeBlond & Mysak (1978). It then follows by superposition that

$$p(r,\theta) = \int_R p(1,\theta_0) G(r,\theta;\theta_0)\,\mathrm{d}\theta_0\,, \tag{3.2}$$

where we recall that the set R corresponds to that portion of the circumference which is rigid, which will typically be of very small spatial extent. To verify this superposition solution, directly differentiating (3.2) shows that $p(r,\theta)$ satisfies the governing equation (2.1) since $G(r,\theta;\theta_0)$ does, while at $r = 1$ substituting (3.1) into (3.2) shows that

$$\frac{\partial p}{\partial r} + \frac{(\omega - Mk)^2}{\mathrm{i}\omega Z} p = \begin{cases} \dfrac{(\omega - Mk)^2}{\mathrm{i}\omega Z} p & \theta \in R \\ 0 & \theta \in L, \end{cases} \tag{3.3}$$

which is the correct boundary condition for both the rigid ($\theta \in R$) and lined ($\theta \in L$) portions.

It is convenient to express $G(r,\theta;\theta_0)$ as the azimuthal Fourier series

$$G(r,\theta;\theta_0) = \sum_{n=0}^{\infty} A_n(r) \cos\big(n(\theta - \theta_0)\big)\,. \tag{3.4}$$

Substituting (3.4) into the governing equation (2.1) shows that we can write $A_n(r)$ in the form

$$A_n(r) = g_n \frac{P_n(r)}{P_n(1)} \qquad\qquad (n \geq 0)\,, \tag{3.5}$$

where $P_n(r)$ is the unscaled solution which is regular at $r = 0$ of the traditional Pridmore–Brown equation

$$\frac{1}{r}\frac{\mathrm{d}}{\mathrm{d}r}\left(r\frac{\mathrm{d}P_n}{\mathrm{d}r}\right) + \frac{2kM'}{\omega - Mk}\frac{\mathrm{d}P_n}{\mathrm{d}r} + \left[(\omega - Mk)^2 - k^2 - \frac{n^2}{r^2}\right] P_n = 0, \tag{3.6}$$

and is such that $P_n(r) = O(r^n)$ as $r \to 0$. Substituting (3.4) into the Green's function

boundary condition (3.1) gives

$$g_n = \frac{\varepsilon_n}{\pi D_n}\,, \qquad\qquad D_n = 1 + \frac{\mathrm{i}\omega Z P_n'(1)}{\big(\omega - M(1)k\big)^2 P_n(1)}\,, \tag{3.7}$$

where $\varepsilon_n = 1$ for $n \neq 0$ and $\varepsilon_0 = 1/2$. Note that the equation $D_n = 0$ is the dispersion relation for waves of azimuthal order n in an unspliced (i.e. fully lined) duct.

Equation (3.6) can in general only be solved numerically, but in the special case of uniform mean flow it reduces to the Bessel equation of order n. It then follows that $P_n(r) = \mathrm{J}_n(\alpha r)$, where J_n is Bessel's function of the first kind of order n and $\alpha^2 = (\omega - Mk)^2 - k^2$, leading to

$$D_n = 1 + \frac{\mathrm{i}\omega Z \alpha \mathrm{J}_n'(\alpha)}{\big(\omega - M(1)k\big)^2 \mathrm{J}_n(\alpha)}\,. \tag{3.8}$$

The dispersion relation $D_n = 0$ matches that for waves in an unspliced duct with uniform mean flow (Rienstra 2003; Brambley & Peake 2006), and its appearance in the denominator (through g_n) of the integral (3.2) mimics the structure of the standard wave Fourier inversion (see, e.g. Lighthill 1978).

3.1. *Solution of the integral equation*

We now proceed to solve the integral equation (3.2) with the geometry shown in figure 1 consisting of two rigid sections, $|\theta| < \varepsilon$ and $|\theta - \pi| < \varepsilon$. In this case, using the Fourier series representation of the Green's function (3.4) gives the integral equation

$$p(1,\theta) = \sum_{n=0}^{\infty} g_n \int_{-\varepsilon}^{\varepsilon} \cos\big(n(\theta-\theta')\big)\big[p(1,\theta') + (-1)^n p(1,\theta'+\pi)\big]\,\mathrm{d}\theta' \qquad \text{for } |\theta| < \varepsilon\,. \tag{3.9}$$

Since there are only certain values of the axial wavenumber k for which a solution to this integral equation exists, we aim to solve (3.9) for $p(1,\theta)$ for $|\theta| < \varepsilon$ with k taking the role of the eigenvalue. The eigenfunction $p(r,\theta)$ is then recovered by

$$p(r,\theta) = \sum_{n=0}^{\infty} g_n \frac{P_n(r)}{P_n(1)} \int_{-\varepsilon}^{\varepsilon} \cos\big(n(\theta-\theta')\big)\big[p(1,\theta') + (-1)^n p(1,\theta'+\pi)\big]\,\mathrm{d}\theta'\,. \tag{3.10}$$

Here, we solve (3.9) by expanding $p(1,\theta)$ as a Fourier series, chosen owing to the simplicity of the algebra. This results in a similar expansion to that used by Fuller (1984), and is equivalently obtained by expanding $1/Z(\theta)$ as a Fourier series. We note, however, that any expansion of $p(1,\theta)$ for $\theta \in (-\varepsilon,\varepsilon)$ could have been used, and indeed other expansions may prove useful either for computational efficiency or in cases where the solution is singular at the edge between the two boundary conditions (unlike here). There are two distinct classes of solutions of (3.9), being when the unsteady pressure is symmetric or antisymmetric in $\theta \to \theta + \pi$, and we address these two cases separately below.

3.1.1. *Symmetric solution*

Here we consider symmetric solutions for which $p(1,\theta+\pi) = p(1,\theta)$. We expand $p(1,\theta)$ as a Fourier series, leading to

$$p(r,\theta) = \sum_{n=0}^{\infty} \frac{P_{2n}(r)}{P_{2n}(1)}\big[a_{2n}\cos(2n\theta) + b_{2n}\sin(2n\theta)\big], \tag{3.11}$$

taking $b_0 = 0$ without loss of generality. Using this Fourier expansion, equation (3.9) then implies

$$\sum_{n=0}^{\infty} a_{2n}\cos(2n\theta) + b_{2n}\sin(2n\theta) \\ = 2\sum_{q=0}^{\infty}\sum_{\ell=0}^{\infty} g_{2q}\int_{-\varepsilon}^{\varepsilon}\cos\big(2q(\theta-\theta')\big)\Big[a_{2\ell}\cos(2\ell\theta') + b_{2\ell}\sin(2\ell\theta')\Big]\,\mathrm{d}\theta'. \quad (3.12)$$

Using standard trigonometric identities gives

$$a_{2n} = 2\varepsilon g_{2n}\sum_{\ell=0}^{\infty} a_{2\ell}\Big(\operatorname{sinc}\big(2(\ell-n)\varepsilon\big) + \operatorname{sinc}\big(2(\ell+n)\varepsilon\big)\Big) \qquad (n\geq 0) \qquad (3.13a)$$

$$b_{2n} = 2\varepsilon g_{2n}\sum_{\ell=0}^{\infty} b_{2\ell}\Big(\operatorname{sinc}\big(2(\ell-n)\varepsilon\big) - \operatorname{sinc}\big(2(\ell+n)\varepsilon\big)\Big) \qquad (n\geq 1), \qquad (3.13b)$$

where $\operatorname{sinc}(z) = \sin(z)/z$ with $\operatorname{sinc}(0) = 1$. Note that in the case $\varepsilon = \pi/2$, equations (3.13a,b) give $a_{2n} = g_{2n}\pi a_{2n}/\varepsilon_n = a_{2n}D_{2n}$ and $b_{2n} = g_{2n}\pi b_{2n} = b_{2n}D_{2n}$, implying that either $a_{2n} = b_{2n} = 0$, or $D_{2n} = 1$ and hence $P'_{2n}(1) = 0$, so that the rigid-wall eigenvalues and eigenfunctions are recovered. Similarly, if $\varepsilon = 0$ then either $a_{2n} = b_{2n} = 0$ or $D_{2n} = 0$, so that the fully lined eigenvalues and eigenfunctions are recovered.

3.1.2. *Antisymmetric solution*

Similarly, considering antisymmetric solutions for which $p(1,\theta+\pi) = -p(1,\theta)$ and setting

$$p(r,\theta) = \sum_{n=0}^{\infty}\frac{P_{2n+1}(r)}{P_{2n+1}(1)}\Big[a_{2n+1}\cos\big((2n+1)\theta\big) + b_{2n+1}\sin\big((2n+1)\theta\big)\Big] \qquad (3.14)$$

leads to

$$a_{2n+1} = 2\varepsilon g_{2n+1}\sum_{\ell=0}^{\infty} a_{2\ell+1}\Big(\operatorname{sinc}\big(2(\ell-n)\varepsilon\big) + \operatorname{sinc}\big(2(\ell+n+1)\varepsilon\big)\Big), \qquad (3.15a)$$

$$b_{2n+1} = 2\varepsilon g_{2n+1}\sum_{\ell=0}^{\infty} b_{2\ell+1}\Big(\operatorname{sinc}\big(2(\ell-n)\varepsilon\big) - \operatorname{sinc}\big(2(\ell+n+1)\varepsilon\big)\Big). \qquad (3.15b)$$

The known results for $\varepsilon = \pi/2$ and $\varepsilon = 0$ are again recovered.

4. Small-ε asymptotics

In this section, we consider the limit of a thin splice $\varepsilon \to 0$. For $\varepsilon = 0$ the duct is uniformly lined, and the problem reduces to the simpler problem of finding the allowable values of k and the corresponding mode shapes $p(r,\theta)$ for a uniformly lined duct (see, e.g., Vilenski & Rienstra 2007); such solutions are of the form $p(r,\theta) = P_q(r)\big(A\cos(q\theta) + B\sin(q\theta)\big)$ with a wavenumber k_0 satisfying $D_q(k_0) = 0$. We now consider small but finite ε for such a mode. Since $D_q(k_0) = 0$, setting $k = k_0 + \varepsilon k_1 + \varepsilon^2 k_2 + \cdots$ gives

$$D_q(k) = \varepsilon D'_q k_1 + \varepsilon^2\left(\frac{1}{2}D''_q k_1^2 + D'_q k_2\right) + \cdots, \qquad (4.1)$$

where a prime here denotes $\partial/\partial k$, so that if $\varepsilon g_q = a + \varepsilon b + \cdots$ then

$$k_1 = \frac{\varepsilon_q}{\pi D'_q a} \qquad\qquad k_2 = -\frac{D''_q \varepsilon_q^2}{2\pi^2 (D'_q)^3 a^2} - \frac{\varepsilon_q b}{\pi D'_q a^2}. \tag{4.2}$$

There are four cases to consider: $A = 0$ or $B = 0$ with q even or q odd. We first derive the asymptotics for the symmetric–symmetric case $B = 0$ with q even, and then proceed to the general case.

4.1. *Symmetric–symmetric asymptotic solution*

Since q is even, we set $q = 2Q$. We choose k_0 such that $D_{2Q}(k_0) = 0$, and pose $a_{2n} = \delta_{nQ} + \varepsilon a'_{2n} + \cdots$ with $b_{2n} \equiv 0$. In this case, the relevant equation to solve is (3.13a), which for $n \neq Q$ gives, to leading order ($O(\varepsilon)$),

$$a'_{2n} = 2g_{2n}(k_0)\Big(\operatorname{sinc}\big(2(Q-n)\varepsilon\big) + \operatorname{sinc}\big(2(Q+n)\varepsilon\big)\Big)\,, \tag{4.3}$$

while (3.13a) with $n = Q$ gives at $O(1)$

$$2a = \big(1 + \operatorname{sinc}(4Q\varepsilon)\big)^{-1} \tag{4.4}$$

and at $O(\varepsilon)$

$$b = -\sum_{\ell\neq Q} g_{2\ell}(k_0) \left(\frac{\operatorname{sinc}\big(2(Q-\ell)\varepsilon\big) + \operatorname{sinc}\big(2(Q+\ell)\varepsilon\big)}{1 + \operatorname{sinc}(4Q\varepsilon)} \right)^2. \tag{4.5}$$

From a and b we may derive the perturbed wavenumber $k = k_0 + \varepsilon k_1 + \varepsilon^2 k_2 + \cdots$ from (4.2), while $a_{2n} = \delta_{nQ} + \varepsilon a'_{2n} + \cdots$ gives the perturbed mode shape $p(r,\theta)$ from (3.11). Note that, at this order, a'_{2Q} is unspecified, and may be taken as zero since this will only affect the normalization of the mode.

4.2. *General asymptotic solution*

Any of equations (3.13a,b) and (3.15a,b) can be expressed in the form

$$c_n = 2\varepsilon y_n \sum_{\ell=0}^{\infty} c_\ell \mathsf{F}_{n\ell}, \tag{4.6}$$

where $\mathsf{F}_{n\ell}$ is a symmetric matrix and $\mathsf{F}_{n\ell}$ and y_n are $O(1)$ except that $y_Q = a/\varepsilon + b + O(\varepsilon)$ for some given Q. For example, for (3.13a) with $D_{2Q}(k_0) = 0$,

$$c_n = a_{2n}, \qquad y_n = g_{2n}, \qquad \mathsf{F}_{n\ell} = \operatorname{sinc}\big(2(\ell-n)\varepsilon\big) + \operatorname{sinc}\big(2(\ell+n)\varepsilon\big). \tag{4.7}$$

Using this notation, we now follow the same method as in §4.1 above. We pose $c_n = \delta_{nQ} + \varepsilon c'_n + \cdots$. For $n \neq Q$, equation (4.6) gives, at leading order,

$$c'_n = 2y_n \mathsf{F}_{nQ}. \tag{4.8}$$

For $n = Q$, equation (4.6) at $O(1)$ and $O(\varepsilon)$ implies

$$a = \frac{1}{2\mathsf{F}_{QQ}}, \qquad\qquad b = -\sum_{\ell\neq Q} y_\ell \frac{\mathsf{F}_{\ell Q}^2}{\mathsf{F}_{QQ}^2} \tag{4.9}$$

This can be seen to reduce to (4.3, 4.4, 4.5) using the definitions of c_n, y_n and $\mathsf{F}_{n\ell}$ from (4.7).

4.3. *Size of perturbation for thin splices*

The uniformly lined duct has two modes for each allowed axial wavenumber k_0, which can be chosen to be $P_q(r)\cos(q\theta)$ and $P_q(r)\sin(q\theta)$. For $\varepsilon \neq 0$ this degeneracy is broken (also seen in Wright 2006), as shown by the different equations satisfied by a_n and b_n for $\varepsilon \neq 0$ (equations (3.13) and (3.15)). Considering first modes with $\cos(2Q\theta)$ dependence governed by (3.13a), for $\varepsilon Q \ll 1$ we find that

$$\mathsf{F}_{QQ} = 1 + \operatorname{sinc}(4Q\varepsilon) = 2 + O\big((Q\varepsilon)^2\big), \tag{4.10}$$

so that a is $O(1)$, and hence the wavenumber perturbation εk_1 is $O(\varepsilon)$. However, for modes with $\sin(2Q\theta)$ dependence, which are governed by (3.13b), we find that

$$\mathsf{F}_{QQ} = 1 - \operatorname{sinc}(4Q\varepsilon) = \frac{8}{3}Q^2\varepsilon^2 + O\big((Q\varepsilon)^4\big), \tag{4.11}$$

so that $a = O(\varepsilon^{-2})$ and hence the wavenumber perturbation $\varepsilon k_1 = O(\varepsilon^3)$, i.e. much smaller than we expected. This difference between the two sets of modes is not surprising, since the two splices lie at pressure zeros of the unperturbed eigenmode $\sin(2Q\theta)$ and can therefore have little effect on the unsteady flow. This result is the same for modes with $q = 2Q + 1$ governed by (3.15).

5. Numerical solution

In the following discussion we consider only symmetric–symmetric modes for which $p(1,\theta) = p(1,-\theta) = p(1,\theta+\pi)$ given by (3.13a), while remarking that the same method gives solutions for the other cases (3.13b, 3.15a,b). We solve (3.13a) numerically by truncating the sum over ℓ to range from 0 to N; in effect, setting $a_{2n} = 0$ for $n > N$. It is hoped that solutions to this finite system will approximate solutions to the infinite system provided that N is sufficiently large. Typically a truncation of $N = 450$ was used in the results that follow.

Define

$$C_i = \frac{1}{2g_{2i}} \qquad \text{and} \qquad \mathsf{F}_{ij} = \operatorname{sinc}\big(2(i-j)\varepsilon\big) + \operatorname{sinc}\big(2(i+j)\varepsilon\big), \tag{5.1}$$

so that F_{ij} is a real symmetric matrix depending only on ε, while the vector C_i depends on k, ω and $M(r)$ but is independent of ε. Setting $\hat{a}_j = a_{2j}$, equation (3.13a) becomes

$$\sum_{j=0}^{N} \mathsf{A}^k_{ij}\hat{a}_j = 0, \qquad \text{where} \qquad \mathsf{A}^k_{ij} = C_i\delta_{ij} - \varepsilon\mathsf{F}_{ij}, \tag{5.2}$$

with the superscript k denoting that A^k is evaluated at k. We wish to solve this using a Newton–Raphson iteration. To avoid the obvious solution of $\hat{a}_i \equiv 0$, we solve the equivalent equation

$$\frac{\mathsf{A}^k\hat{\boldsymbol{a}}}{\sqrt{\langle\hat{\boldsymbol{a}},\hat{\boldsymbol{a}}\rangle}} = 0, \qquad \text{where} \qquad \langle\boldsymbol{x},\boldsymbol{y}\rangle = \sum_{i=0}^{N}\overline{x_i}y_i = \overline{\boldsymbol{x}}^T\boldsymbol{y}, \tag{5.3}$$

with $\overline{x_i}$ denoting the complex conjugate of x_i. For small $\boldsymbol{\delta a}$ and δk, taking $\boldsymbol{\delta a} = \lambda\hat{\boldsymbol{a}} + \boldsymbol{\delta a}^*$ with $\langle\hat{\boldsymbol{a}},\boldsymbol{\delta a}^*\rangle = 0$ gives

$$\frac{\mathsf{A}^{k+\delta k}(\hat{\boldsymbol{a}}+\boldsymbol{\delta a})}{\big(\langle\hat{\boldsymbol{a}}+\boldsymbol{\delta a},\hat{\boldsymbol{a}}+\boldsymbol{\delta a}\rangle\big)^{1/2}} = \frac{1}{\sqrt{\langle\hat{\boldsymbol{a}},\hat{\boldsymbol{a}}\rangle}}\Big(\big(1+\mathrm{i}\mathrm{Im}(\lambda)\big)\mathsf{A}^k\hat{\boldsymbol{a}} + \mathsf{A}^k\boldsymbol{\delta a}^* + \delta k\,\big(\mathsf{A}^k\big)'\hat{\boldsymbol{a}}\Big) + O\left(\langle\boldsymbol{\delta a},\boldsymbol{\delta a}\rangle,\delta k^2\right), \tag{5.4}$$

where a prime denotes $\partial/\partial k$. Note that the value of $\mathrm{Re}(\lambda)$ has no effect on this expression, while $\mathrm{Im}(\lambda)$ will only affect the normalization of our solution, and so we take $\lambda = 0$. Our Newton–Raphson iteration therefore consists of choosing $\boldsymbol{\delta a}^*$ and δk such that

$$\mathsf{A}^k \boldsymbol{\delta a}^* + \delta k \left(\mathsf{A}^k\right)' \hat{\boldsymbol{a}} = -\mathsf{A}^k \hat{\boldsymbol{a}}. \tag{5.5}$$

We must proceed carefully in solving (5.5), since we seek an eigenvalue k such that A is noninvertible. First, we project (5.5) onto a basis orthogonal to $\hat{\boldsymbol{a}}$, since we know $\boldsymbol{\delta a}^*$ to be orthogonal to $\hat{\boldsymbol{a}}$ and we seek an $\hat{\boldsymbol{a}}$ lying in the kernel of A. To do this, we choose q such that $|\hat{a}_q| \geq |\hat{a}_i|$ for all i and set

$$\boldsymbol{\delta a}^* = \sum_{i \neq q} b_i \left(\boldsymbol{e}_i - \frac{\langle \hat{\boldsymbol{a}}, \boldsymbol{e}_i \rangle}{\langle \hat{\boldsymbol{a}}, \hat{\boldsymbol{a}} \rangle} \hat{\boldsymbol{a}} \right), \tag{5.6}$$

where $\boldsymbol{e}_i$ are the standard basis vectors so that $\hat{\boldsymbol{a}} = \sum_{i=0}^{N} \hat{a}_i \boldsymbol{e}_i$. Replacing the qth component of our system of N equations with the δk equation transforms (5.5) into

$$\mathsf{B}\Big(b_0, \cdots, b_{q-1}, \delta k, b_{q+1}, \cdots, b_N\Big)^T = -\mathsf{A}^k \hat{\boldsymbol{a}}, \tag{5.7a}$$

where

$$\mathsf{B}_{ij} = \begin{cases} \langle \boldsymbol{e}_i, \left(\mathsf{A}^k\right)' \hat{\boldsymbol{a}} \rangle & j = q \\ \mathsf{A}^k_{ij} - \dfrac{\langle \boldsymbol{e}_i, \mathsf{A}^k \hat{\boldsymbol{a}} \rangle}{\langle \hat{\boldsymbol{a}}, \hat{\boldsymbol{a}} \rangle} \overline{\hat{a}_j} & j \neq q. \end{cases} \tag{5.7b}$$

We assume B to be invertible, and so inversion gives b_i and δk, from which $\boldsymbol{\delta a} = \boldsymbol{\delta a}^*$ can be recovered from (5.6).

In summary, the Newton–Raphson step is to form the matrix B given in (5.7), to solve $\mathsf{B}\boldsymbol{b} = -\mathsf{A}^k \hat{\boldsymbol{a}}$, and then to update $\hat{\boldsymbol{a}} \to \hat{\boldsymbol{a}} + \boldsymbol{\delta a}$ and $k \to k + \delta k$; here, the LAPACK routine ZGESV was used for the inversion (Anderson *et al.* 1999). As a starting point for the iteration we choose a mode of order $m = 2Q$ of the unspliced problem with eigenvalue k_0, so that our initial guess is $k = k_0$ and $\hat{a}_i = \delta_{iQ}$. Alternatively, $\hat{a}_i = \delta_{iQ}$ and a random value of k may be taken, or the asymptotic prediction above may be used for an initial guess at k and $\hat{\boldsymbol{a}}$.

The above procedure typically converges reasonably quickly. For example, for $\omega = 31$, $Z = 2 + \mathrm{i}$ and $M \equiv 0.5$, finding all eigenvalues with $|\mathrm{Im}(k)| < 50$ for $\varepsilon = 0.1$ that are the equivalent of $m = 24$ unspliced eigenvalues took 16 seconds on a 3GHz quad-core desktop computer; evaluating the asymptotics of §4 for the same case was instant.

5.1. *Solution of $P_n(r)$*

Calculating C_i above involves calculating $P'_{2i}(r)/P_{2i}(r)$. For a general flow profile $M(r)$, this was performed by solving the Pridmore–Brown equation (3.6) using the same code as Brambley (2011*b*), which is a 12th order implicit central finite-difference scheme on unevenly spaced collocation points, allowing points to be clustered in regions of interest, such as boundary layers. The boundary conditions applied were $P'_0(0) = 0$ or $P_n(0) = 0$ for $n \neq 0$, and $P_n(1) = 1$ for all n. This yielded a banded matrix, which was solved using the LAPACK routine ZGBSV (Anderson *et al.* 1999). Typically $N_n = 2000$ collocation points where used.

For uniform mean flow, $P_n(r) = \mathrm{J}_n(\alpha r)$ with $\alpha^2 = (\omega - Mk)^2 - k^2$. In this case no finite-difference scheme is needed, and here the algorithm of Amos (1986) was used to compute J_n. However, since we are interested only in the ratio of $P'_n(\alpha)/P_n(\alpha)$, care must be taken to avoid numerical underflow and overflow. It was found necessary to

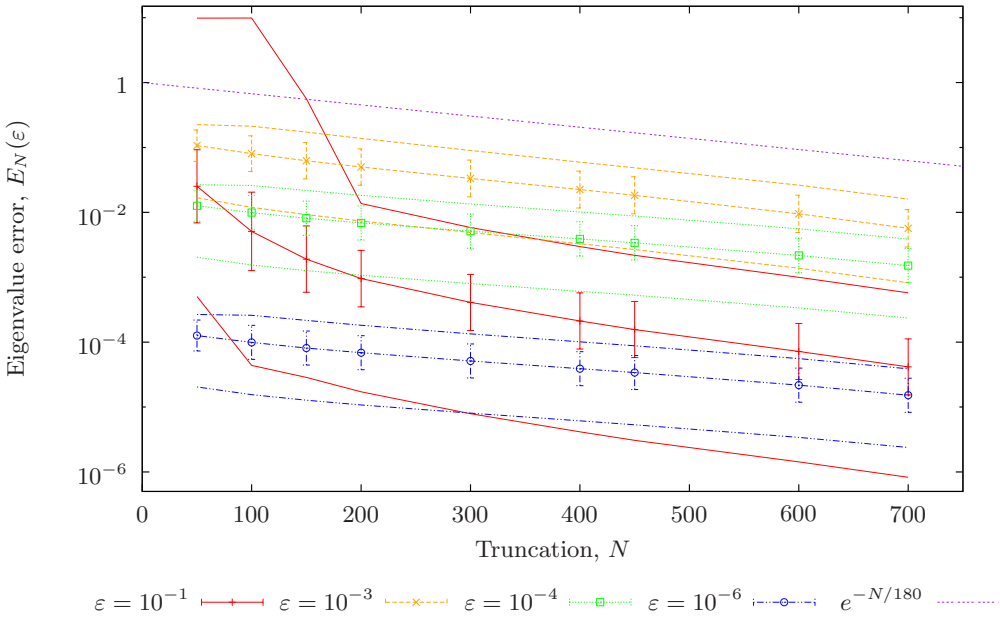

FIGURE 2. Accuracy of numerical eigenvalues k_N as the numerical truncation N is varied, for various splice widths ε. Plotted are minimum, maximum, and (geometric) averages of the eigenvalue error $E_N^i(\varepsilon)$ (defined in equation 5.11) for all eigenvalues with $|\mathrm{Im}(k^i(\varepsilon))| < 200$, with error bars showing one standard deviation. Also plotted is a reference line $e^{-N/180}$. Here $\omega = 31$, $M \equiv 0.5$, $Z = 2 + \mathrm{i}$ and $m = 24$.

supplement the algorithm of Amos by the following when $m \gg 1$,

$$z\frac{P_n'(z)}{P_n(z)} = m - 2(m+1)\frac{\displaystyle\sum_{i=0}^{\infty} \frac{\left(-z^2/4\right)^i}{i!(i+m)!/m!}}{\displaystyle\sum_{i=0}^{\infty} \frac{\left(-z^2/4\right)^i}{i!(i+m+1)!/(m+1)!}} \qquad \text{when } |z|^2 < 4(m+1), \quad (5.8)$$

$$mz\frac{P_n'(mz)}{P_n(mz)} \sim -m^{2/3}\sqrt{\left(1-z^2\right)/\zeta}\,\frac{\mathrm{Ai}'\left(m^{2/3}\zeta\right)}{\mathrm{Ai}\left(m^{2/3}\zeta\right)} \qquad \text{otherwise,} \quad (5.9)$$

where Ai is the Airy function of the first kind and

$$\frac{2}{3}\zeta^{3/2} = \log\left(\left(1+\sqrt{1-z^2}\right)/z\right) - \sqrt{1-z^2}, \quad (5.10)$$

the branch being chosen such that ζ is real for real z. For details, see Abramowitz & Stegun (1964, ch. 9).

5.2. *Validation of numerics and asymptotics*

For uniform mean flow, figure 2 shows how the normalized error for the numerically calculated eigenvalues varies with the numerical truncation N for different values of ε. For each eigenvalue $k^i(\varepsilon)$, let $k_N^i(\varepsilon)$ be the corresponding numerically calculated eigenvalue

ε	A	B
10^{-1}	2×10^{-3}	180
10^{-3}	0.11	250
10^{-4}	1.2×10^{-2}	350
10^{-6}	1.2×10^{-4}	350

TABLE 1. Coefficients for $E_N(\varepsilon) = Ae^{-N/B}$ that give best-fit lines matching the average errors shown in figure 2 for different splice widths ε.

for a numerical truncation N. We define the normalized error for this eigenvalue as

$$E_N^i(\varepsilon) = \frac{|k_N^i(\varepsilon) - k_{1000}^i(\varepsilon)|}{|k_{1000}^i(\varepsilon) - k^i(0)|}, \tag{5.11}$$

so that $E_N^i(\varepsilon)$ is the discrepancy in position of eigenvalue i between this truncation and a truncation of 1000 normalized by the distance the eigenvalue moves from fully lined ($\varepsilon = 0$) to the given splice width; a small value of $E_N^i(\varepsilon)$ compared with 1 therefore implies the effect of the splice has been well resolved. From the reference line $e^{-N/180}$ plotted in figure 2, the eigenvalue error can be seen to decay exponentially with increasing N; for this example, table 1 gives the coefficients for best fit exponential decay fitted to the average error curves of figure 2. The worst numerical convergence is seen for $\varepsilon \approx 10^{-3}$. That the worst numerical convergence is found not for large or small ε but for some intermediate value may be explained, as for very small ε all off-diagonal terms in A_{ij}^k are very small (and there would be zero truncation error if A were diagonal), while for larger ε the off-diagonal terms decay faster with increasing N. The value of $N = 450$ used for all results presented here ensures an accuracy $E_N < 0.05$ for $|\mathrm{Im}(k)| < 200$ for all values of ε considered. While it is expected that this numerical truncation will be sufficient for all impedances Z but is likely to need increasing for higher frequencies than the $\omega = 31$ considered here, this will not be investigated further.

Again for uniform mean flow, figure 3 shows the accuracy of the asymptotics from §4.1 compared with the numerical results calculated using the algorithm above, for the aeroacoustically relevant parameters $\omega = 31$, $m = 2Q = 24$, $M \equiv 0.5$ and $Z = 2 + \mathrm{i}$, with the numerics performed using a truncation of $N = 450$. The theoretical order of accuracy of the asymptotics is recovered (as seen from figure 3*a*), giving confidence in the correctness of both the asymptotics and the numerics. A similar result is recovered from consideration of the a_n coefficients instead of the axial wavenumber k.

6. Results

Figure 4 shows some eigenvalues in the k-plane for the parameters used in §5.2 with $\varepsilon = 0.1$, and compares the unspliced and spliced eigenvalues. Note that, while the large imaginary axis range causes modes to look compressed, in fact all modes are discrete, with no continuous spectrum being present owing to the uniform mean flow used. On the scale of the figure, the effect of the splice on the eigenvalues is seen to be small, although this will be discussed in detail later in this section; in contrast, the effect on the mode shapes will be seen to be very significant. The eigenfunctions for the modes labelled k_+, k_- and k_{HI} (which are typical of the results for the other modes) are given in figures 5, 6 and 7 respectively. Comparing figures 5 and 6 suggests that the effect of the splice is more significant for upstream-propagating modes (k_- in figure 6*b*) than for downstream-

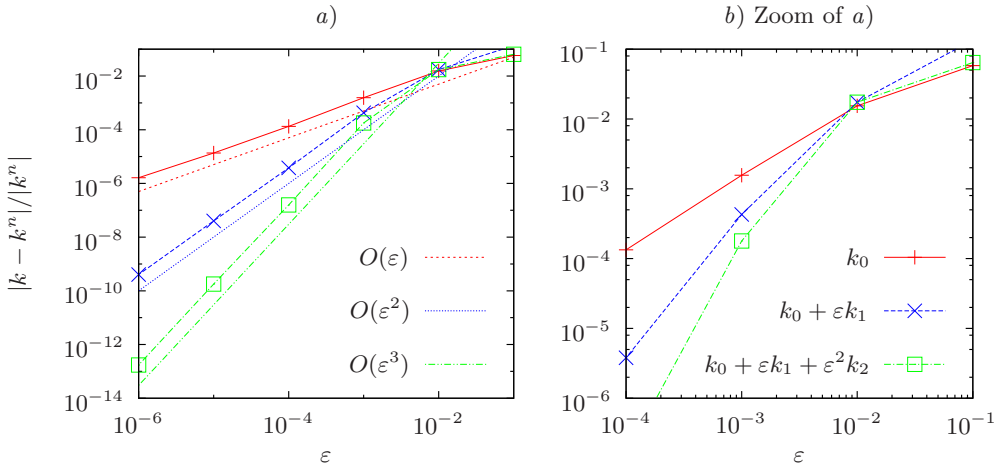

FIGURE 3. Average accuracy of asymptotic small-ε eigenvalue prediction of k from (4.4), (4.5) and (4.2), averaged over all resolved modes with $|\mathrm{Im}(k_0)| < 400$. The numerical eigenvalue is k^n for $N = 450$. Here $\omega = 31$, $M \equiv 0.5$, $Z = 2 + \mathrm{i}$ and $m = 24$. Figure b) shows a closer view of the top right of a).

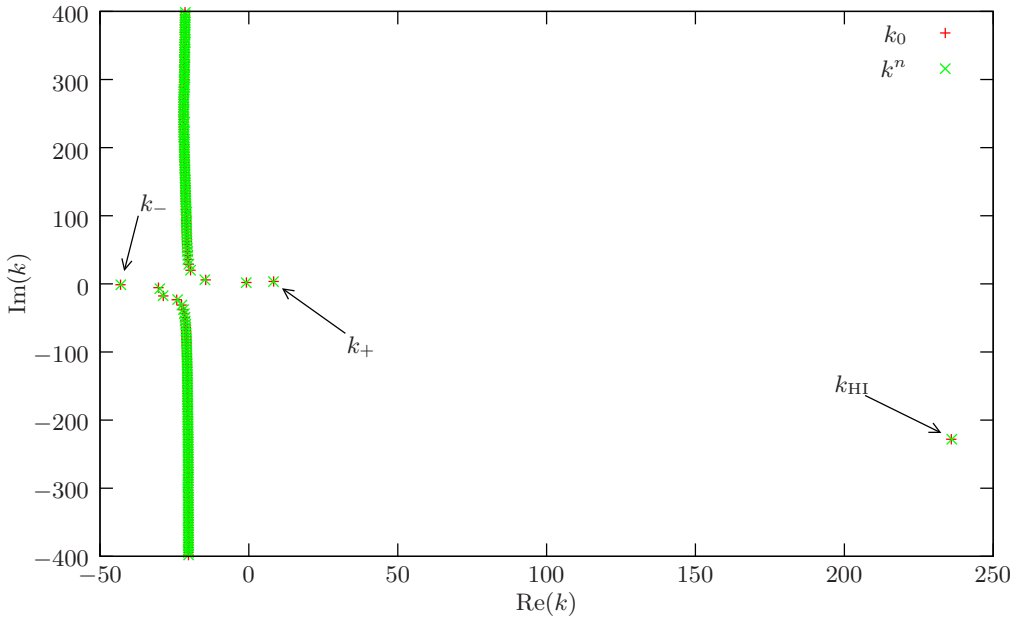

FIGURE 4. Unspliced eigenvalues (k_0, +) and numerical eigenvalues (k^n, ×) for $\varepsilon = 0.1$ and $N = 450$, plotted in the k-plane. Here $\omega = 31$, $M \equiv 0.5$, $Z = 2+\mathrm{i}$ and $m = 24$. The eigenfunctions for the three modes labelled k_+, k_- and k_{HI} are given in figures 5, 6 and 7.

propagating modes (k_+ in figure 5b). Since the hydrodynamic instability eigenfunction for $k = k_{\mathrm{HI}}$ is difficult to see, being concentrated close to the boundary (as befits its description as a surface mode), it is shown in r, θ coordinates. It is interesting to note that the surface mode appears to be sustained by the lining and is exactly cancelled out on the splice.

Turning now to how the modes vary from uniformly lined as ε is increased from zero,

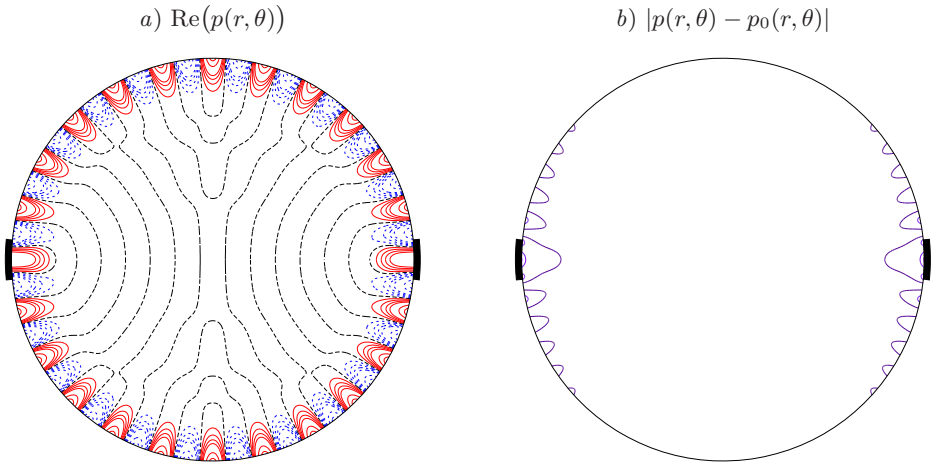

FIGURE 5. Contours of the eigenfunction $p(r,\theta)$ for $k = k_+$ (as shown in figure 4), normalized so that $\max|p(r,\theta)| = 1$. Contours are spaced at 0.1, 0.2, 0.3, 0.4, 0.7, and 0.9. The thick black marks around the outside represent the locations of the two splices. *a*) $\mathrm{Re}(p(r,\theta))$. Solid contours are positive, dotted contours are negative, and the dashed contour is the zero contour. *b*) The deviation of the spliced mode from the unspliced mode, $|p(r,\theta) - p_0(r,\theta)|$. Here $\varepsilon = 0.1$, $\omega = 31$, $M \equiv 0.5$, $Z = 2 + \mathrm{i}$, $m = 24$ and $N = 450$.

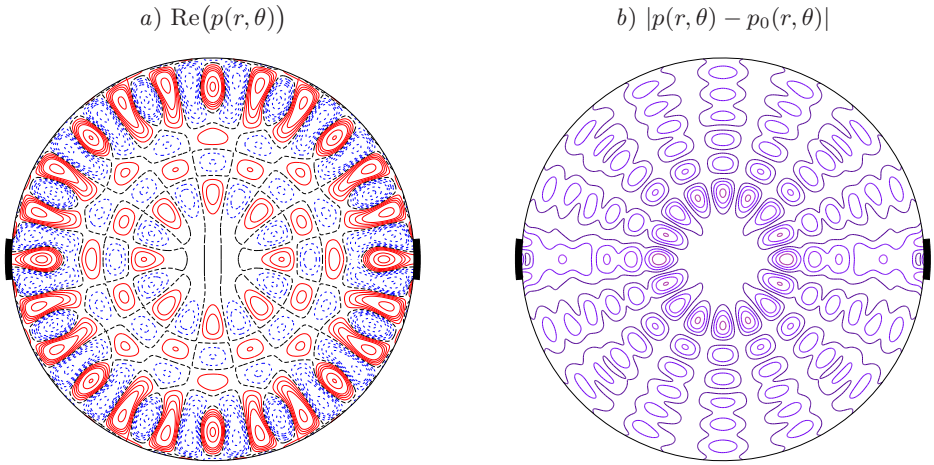

FIGURE 6. As for figure 5 but for $k = k_-$.

figure 8 shows the movement in the k-plane as ε is varied from 0 to 0.1 for the same parameters as figure 4. Interestingly, figure 8*b*) shows that for the upstream-propagating k_- mode, increasing the splice width initially causes an increase in the damping provided by the lining for both the even (3.13*a*) and odd (3.13*b*) modes, although further increasing the splice width leads to decreased damping owing to a smaller area of liner. For the downstream-propagating equivalent k_+ mode shown in figure 8*c*), any nonzero splice width leads to a decrease in damping. The surface mode k_{HI} shown in figure 8*d*) shows an interesting similarity between the even and odd modes apart from for very small values

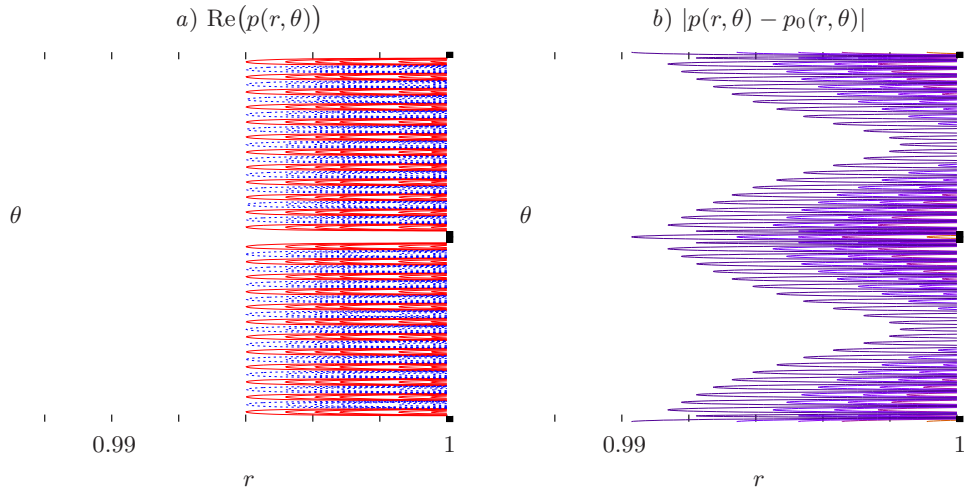

FIGURE 7. As for figures 5 and 6 but for $k = k_{\mathrm{HI}}$, plotted in r, θ axes. The locations of the splices are shown by the boxes on the right of the figures.

of ε. As $\varepsilon \to \pi/2$, k_{HI} tends to infinity since it is not supported by the fully rigid-walled duct corresponding to $\varepsilon = \pi/2$.

6.1. *Azimuthal Fourier modal amplitudes*

The pressure within the duct is given as an azimuthal Fourier sum in (3.11) and (3.14). For the unspliced duct with $\varepsilon = 0$ we consider modes of azimuthal order m for which $a_n = \delta_{mn}$ with $b_n = 0$ (where we are here considering modes with $\cos(m\theta)$ dependence, although modes with $\sin(m\theta)$ dependence may be treated in the same way). As ε is increased, we keep $a_m = 1$ fixed and allow the other components and the axial wavenumber k to vary smoothly (as in figure 8). In this way, we end up with the azimuthal modal amplitudes a_n and a value of k for $\varepsilon = 0.1$. We now show results for the amplitudes a_n for these modes.

For the k_+ mode identified in figure 4 (azimuthal order $m = 24$, with $\varepsilon = 0$), the azimuthal modal amplitudes are shown in figure 9. The dominant azimuthal order can be seen to still be $m = 24$ when $\varepsilon = 0.1$, as might have been expected from its mode shape shown in figure 5. In contrast, figure 10 shows the corresponding result for the k_- mode identified in figure 4 when $\varepsilon = 0.1$. While the a_{24} coefficient is still significant, the dominant contribution now comes from the a_8 azimuthal mode, with modes a_6, a_{16} and a_{20} also being important, among others. This leads to the more complicated modal shape for this mode shown in figure 6, with the eight-fold symmetry in the centre clearly visible. This demonstrates the rather surprising result that the spliced equivalent of the unspliced $m = 24$ order mode need not be dominated by the a_{24} azimuthal mode, even for ε as small as 0.1. This result is also emphasized by figure 11, which shows the equivalent for the k_{HI} mode from figure 4. A cursory examination of figure 11 might suggest that the tracking of this particular mode from $\varepsilon = 0$ to $\varepsilon = 0.1$ became confused and instead, at some point, picked up the $m = 26$ mode. However, a careful investigation of the variation of the a_n coefficients as ε is varied shows that this is not the case; indeed, the track of the $m = 26$ k_{HI} mode does not intersect with that of the $m = 24$ k_{HI} mode for $\varepsilon \in [0, 0.1]$.

We will return to the asymptotics plotted in figures 9–11 in §6.4.

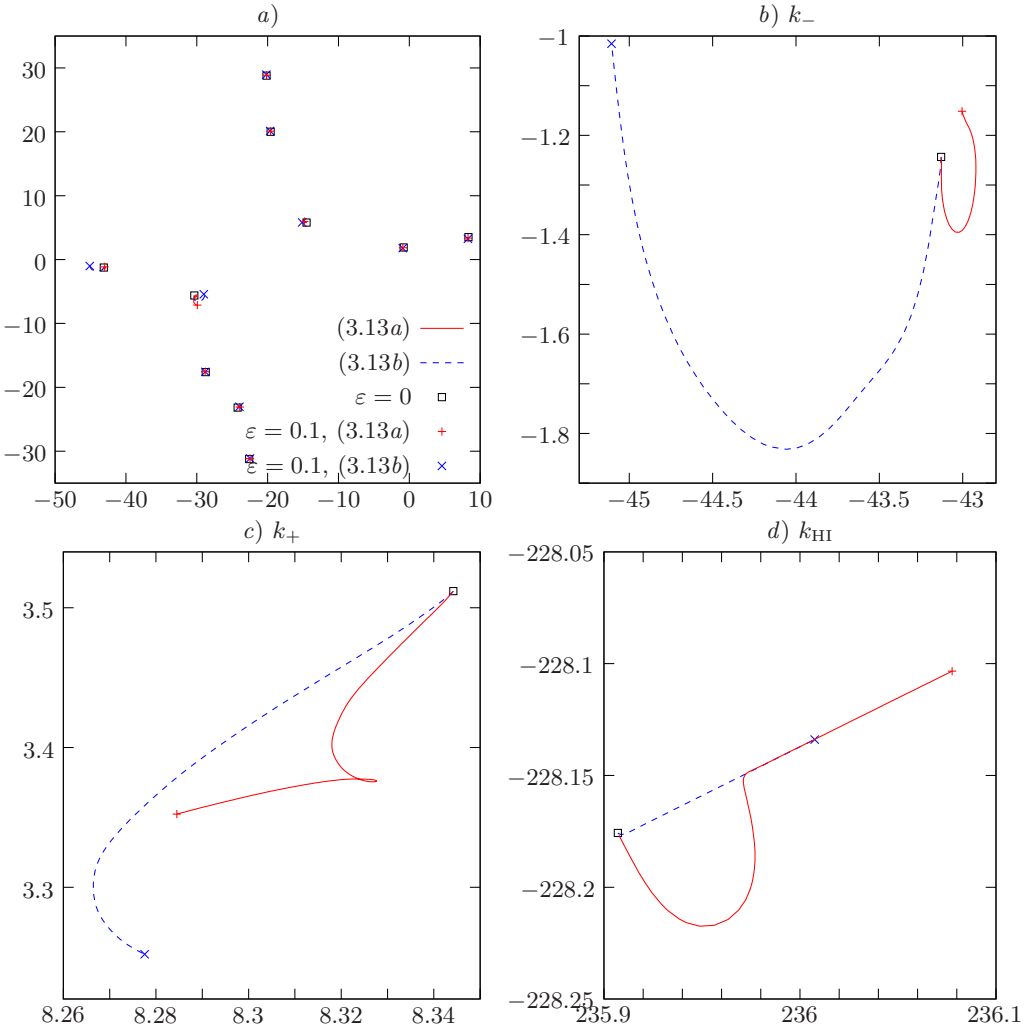

FIGURE 8. Trajectories of modes in the k-plane as ε is varied from 0 to 0.1. Figure a) demonstrates the relatively small changes due to the splice, b) and c) show enlargements of the leftmost (k_-) and rightmost (k_+) modes respectively, while d) shows an enlargement of the surface mode k_{HI} (which is not shown in figure a) owing to the scale used). Parameters are as for figure 4.

6.2. *Thin sheared boundary layer flow*

Here we consider a sheared mean flow that differs from the uniform flow only in a thin boundary layer of width δ. The boundary layer profile used here is the tanh profile used by Rienstra & Vilenski (2008),

$$M(r)/M_0 = \tanh\left(\frac{1-r}{\delta}\right) + \big(1-\tanh(1/\delta)\big)\left(\frac{1+\tanh(1/\delta)}{\delta}r + (1+r)\right)(1-r). \quad (6.1)$$

For a centreline Mach number of $M_0 = 0.5$ and a thin boundary layer of width $\delta = 10^{-3}$, the trajectories of modes in the k-plane as ε is varied from 0 to 0.1 are shown in figure 12 together with the trajectories of modes in a uniform mean flow (taken from figure 8). The effect of the thin boundary layer is shown to be of comparable magnitude to the effect of the splice for most modes. Note, however, that figures 8d) and 12d) show modes

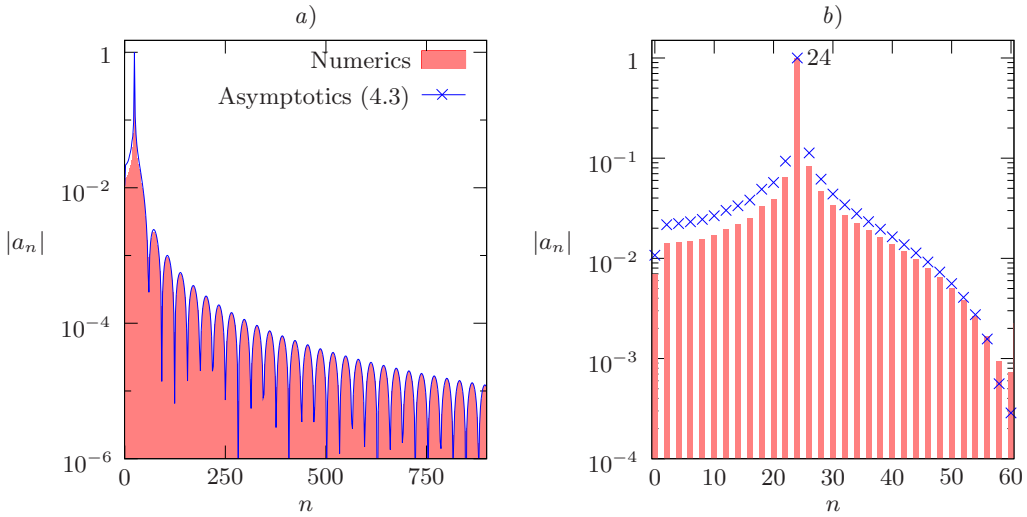

FIGURE 9. Azimuthal modal amplitudes a_n from (3.11), for the k_+ mode shown in figure 4. This mode originated for $\varepsilon = 0$ as a mode with azimuthal order $m = 24$. *b*) is a more detailed view of *a*). Also shown is the asymptotic prediction from (4.3). Parameters are as for figure 4.

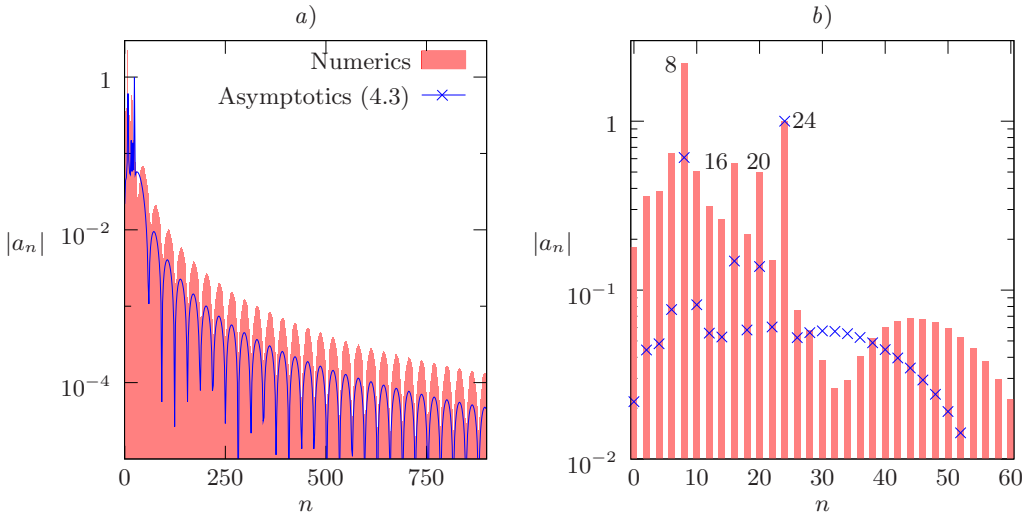

FIGURE 10. The same as figure 9 but for the k_- mode shown in figure 4.

in totally different areas of the k-plane. There is no equivalent of the uniform-flow k_{HI} mode for this sheared flow profile; instead, however, there is a new mode here labelled k_{BL} which was not present with uniform flow. It should be emphasized that this mode is not just the k_{HI} mode in a different quadrant of the k-plane, but rather a new mode totally separate from k_{HI}; this can be verified by tracking the location of modes for a flow profile of $\eta M(r) + (1-\eta)M_0$ as η is smoothly varied from 0 to 1.

6.3. *Parabolic sheared flow*

Here we consider a parabolic profile given by

$$M(r) = M_0\big(1 - r^2\big). \tag{6.2}$$

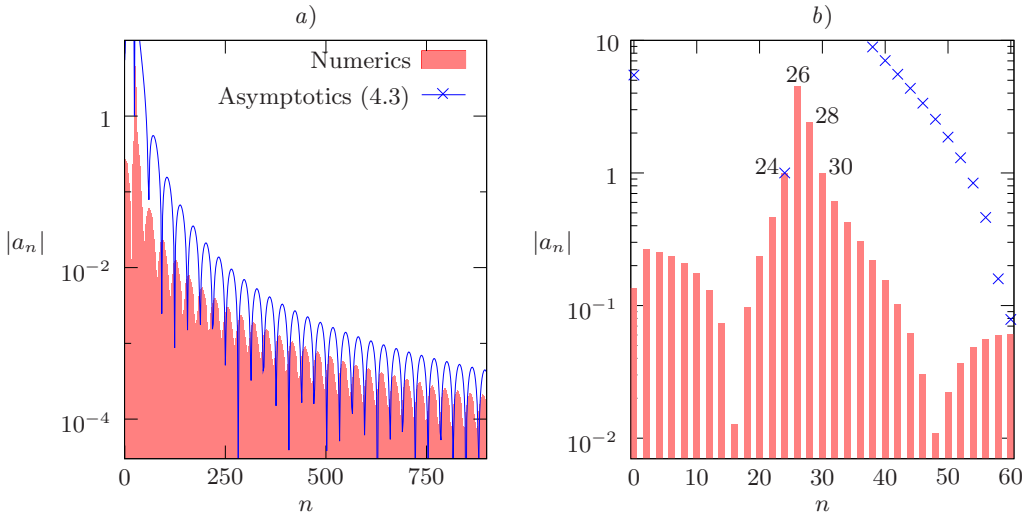

FIGURE 11. The same as figure 9 but for the k_{HI} mode shown in figure 4.

For $M_0 = 0.5$, the motion of the axial wavenumber k in the k-plane as ε is varied from 0 to 0.1 is shown in figure 13. Note that for this situation, both the upstream-propagating first-order mode k_+ and the downstream-propagating first-order mode k_- become less damped for increasing splice width ε, at least up until $\varepsilon = 0.1$. This is in contrast to the uniform or thin-boundary-layer profiles shown in figures 8 and 12, for which the upstream-propagating first-order mode k_- is initially more damped with a thin splice than with no splice at all. For this case there is neither a k_{HI} nor a k_{BL} mode.

6.4. *Comparison of asymptotics and numerics*

Also plotted in figure 13 are the asymptotic predictions from §4, both for the sin and cos type modes and for the first- and second-order asymptotics. While this is shown for just two modes and for a parabolic flow profile, these graphs are typical of all flow profiles and modes considered. The first-order predictions for the sin and cos modes are in the same direction but of different magnitudes, as predicted in §4.3. This shows the practicality of using the first-order asymptotics from §4 for thin splices to predict whether a splice will increase or decrease the damping of a given mode, and also the practicality of using the second-order asymptotics to get an estimate of the magnitude of such a change in damping.

Figures 9–11 showing the modal composition of the k_+, k_- and k_{HI} modes for $\varepsilon = 0.1$ also show the predicted modal amplitudes from the asymptotics given in (4.4). As can be seen, the prediction for the k_+ mode in figure 9 is quantitatively correct, while the predictions for the k_- and k_{HI} modes in figures 10 and 11 are not. We note that these modal composition inaccuracies could lead to errors when used for mode-matching, although for smaller values of ε (say $\varepsilon \leq 0.01$) the asymptotics may well be sufficiently accurate for mode-matching applications. For the k_- mode at $\varepsilon = 0.1$, however, it could still be argued that the asymptotic prediction is qualitatively correct, in that it correctly predicts the importance of the 8th, 16th and 20th azimuthal order modes; moreover, since the asymptotic correction to the 24th order mode was unspecified by the asymptotics and was taken to be zero (remembering that $q = 24$ in this case), it is perhaps understandable that the relative magnitude of the 24th order modes is less well predicted compared with that of the others. However, the asymptotic prediction of the k_{HI} mode shown in figure 11

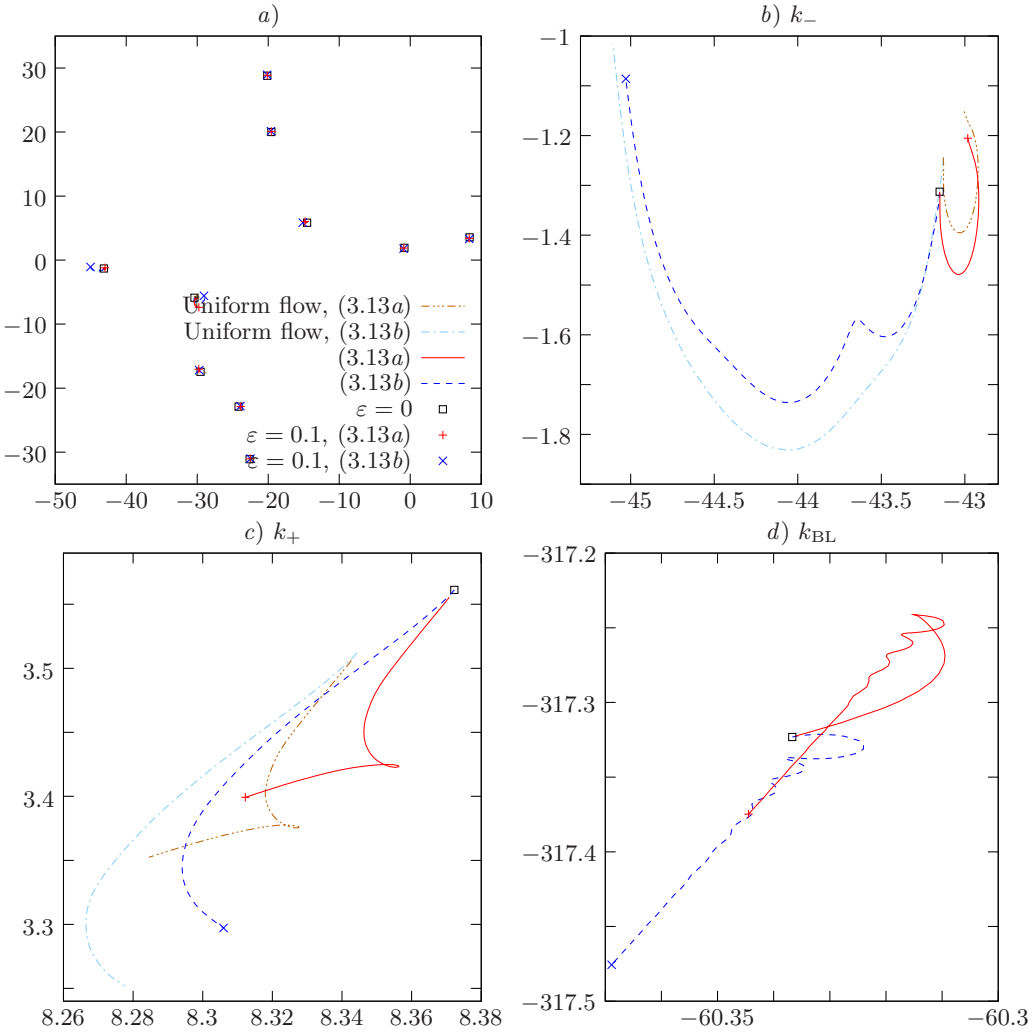

FIGURE 12. Trajectories of modes in the k-plane as ε is varied from 0 to 0.1, similar to figure 8 but for a thin boundary layer sheared flow given by (6.1) with $M_0 = 0.5$ and $\delta = 10^{-3}$. Also shown are the uniform-flow trajectories from figure 8. In *d*), k_{BL} is a thin boundary layer surface mode with no uniform-flow equivalent; the k_{HI} mode is not present for this flow profile. Here $\omega = 31$, $Z = 2 + \mathrm{i}$, $m = 24$, $N_n = 2000$ and $N = 450$.

is not even qualitatively correct. This appears to be a general trend, since numerous numerical calculations have shown that ε needs to be extremely small (of the order of 10^{-4} for the parameters used for these figures) for the asymptotics to be accurate for surface modes. One reason for this could be that the asymptotics require the splice to be thin compared with the appropriate radial lengthscale of the mode, and this radial lengthscale is very small for surface modes which are by their nature highly localized about the boundary.

6.5. *Trapped Modes*

We now turn our attention to *trapped modes*, as discovered by Bi *et al.* (2009) for a single splice without flow. Trapped modes are modes which are localized within the immediate neighbourhood of a splice. Bi *et al.* found that they originate as unspliced surface modes

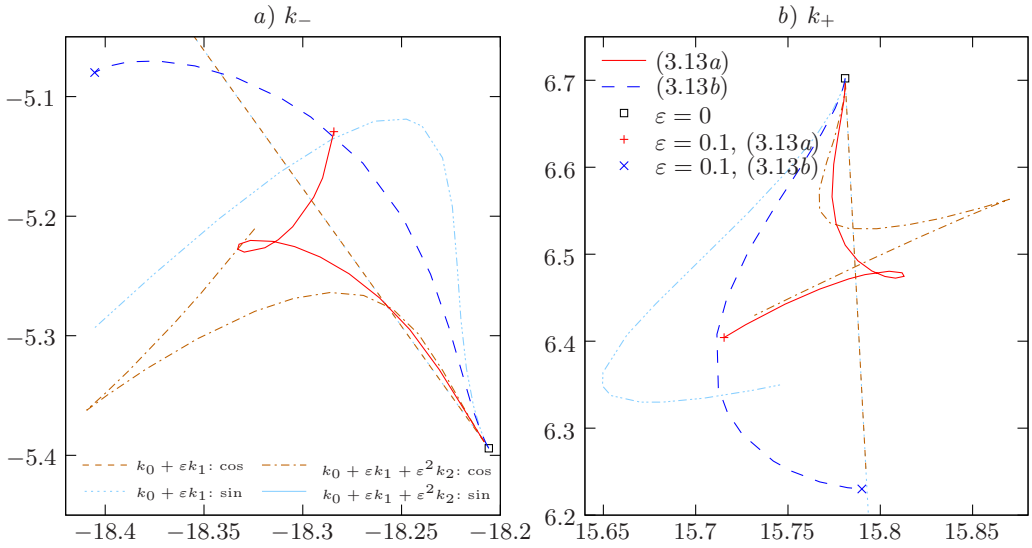

FIGURE 13. Trajectories of modes in the k-plane as ε is varied from 0 to 0.1, similar to figure 8 but for a parabolic boundary layer profile given by (6.2). Also shown are the first- and second-order asymptotics from (4.2). Here $M_0 = 0.5$, $\omega = 31$, $Z = 2 + \mathrm{i}$, $m = 24$, $N_n = 2000$ and $N = 450$.

of low order, and turn into acoustic propagating modes as the splice width is increased; it is for thin splices where they are undergoing this transition that they appear as trapped modes.

Figure 14 shows the same case as considered by Bi *et al.* but for two symmetric splices rather than the single splice they considered. (Note that Bi *et al.* also considered a smoothly varying admittance $1/Z(\theta)$ with a Gaussian profile for the splice, while here we consider a step function impedance varying abruptly from lined to rigid.) For these parameters, Bi *et al.* found that the trapped mode originates as an unspliced surface mode of azimuthal order $m = 0$. Here, owing to the different splice geometry, we find the trapped mode occurring for $m = 2$. Figure 14*a* shows the evolution of the trapped mode from an $m = 2$ surface mode for $\varepsilon = 0$ with non-negligible $\mathrm{Im}(k)$ to a trapped mode (figures 14*c,e*) as ε is increased, and finally to an almost fully acoustic mode with a significantly reduced $\mathrm{Im}(k)$ for $\varepsilon = 0.1$. Since there is no flow in this case, the behaviour is symmetric in x and the other surface mode similarly becomes a trapped mode running in the other direction.

Also shown in figure 14 is the accuracy of the small-ε approximation from §4.1. Figure 14*a* shows the full trajectory in the k-plane as ε is varied from 0 to 0.1, and demonstrates that the asymptotics is not quantitatively correct for moderately small ε in this case. However, the small-ε asymptotics does correctly reproduce the quantitative behaviour for sufficiently small ε, as it must, and indeed this is shown in figure 14*b*. The corresponding eigenfunctions for this mode for $\varepsilon = 0.005$ are compared in figures 14*c,d*, and show a marked similarity. For $\varepsilon = 0.05$ the accuracy of the asymptotics is not as good, as shown in figures 14*e,f* and as expected from the significantly different predictions for the eigenvalue k; nonetheless, the qualitative behaviour of having maximal amplitude on the splice is captured by the asymptotics.

Introducing a uniform mean flow of Mach number $M \equiv 0.5$ gives the situation shown in figure 15. Concentrating first on the eigenvalues k shown in figure 15*a* for both $m = 0$ and $m = 2$, it is obvious that the upstream–downstream symmetry is broken by the mean flow. The downstream-propagating trapped mode originating as a surface mode for

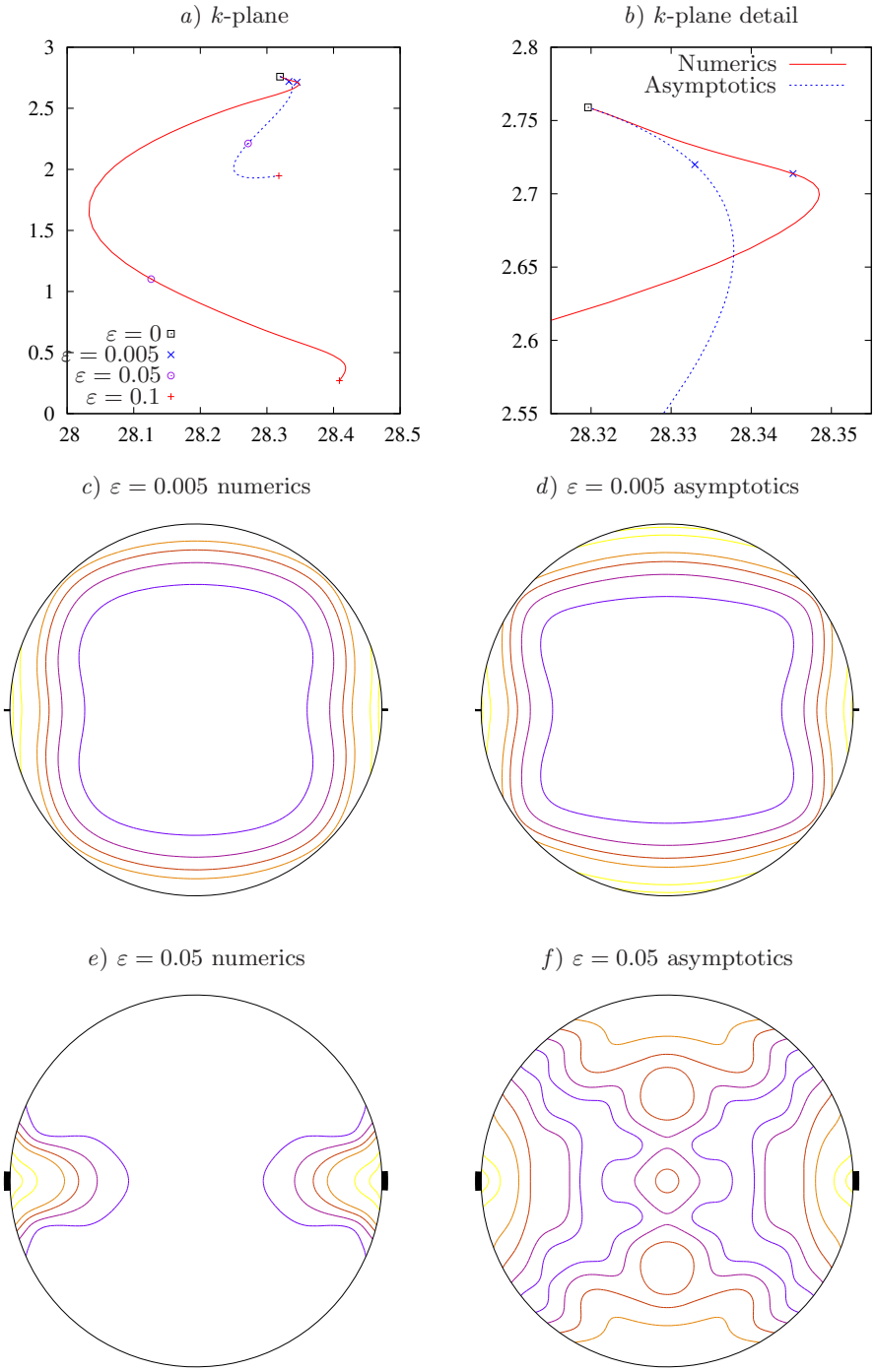

FIGURE 14. Accuracy of the asymptotics for trapped modes without flow. Here $M = 0$, $Z = 2+\mathrm{i}$, $\omega = 30$ and $m = 2$. Contour plots are of $|p(r, \theta)|$, with contours at 0.1, 0.2, 0.3, 0.4, 0.7 and 0.9 of the maximum magnitude.

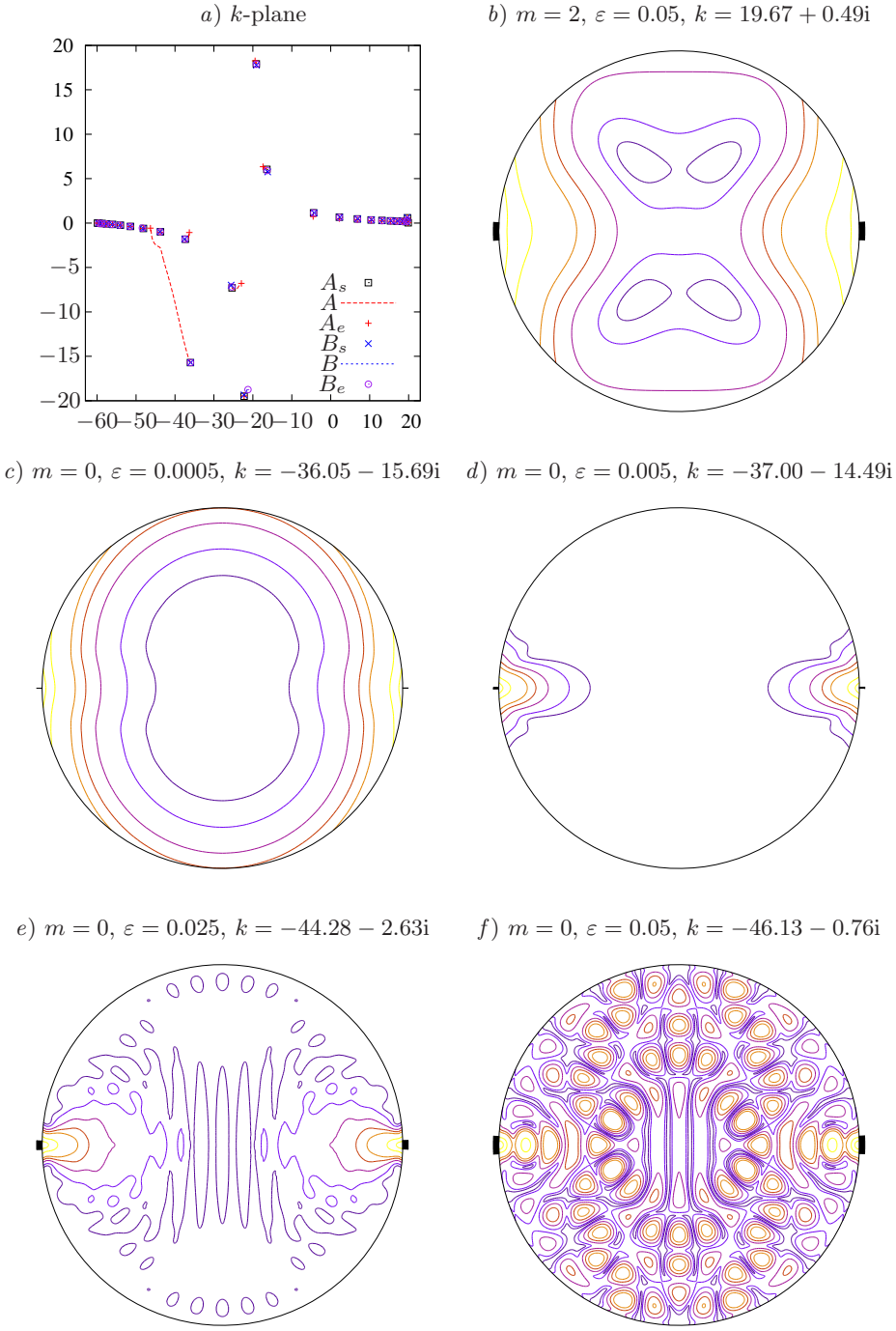

FIGURE 15. Trapped modes with uniform flow with $m = 0$ when $\varepsilon = 0$ (labelled A) and with $m = 2$ when $\varepsilon = 0$ (labelled B), from $\varepsilon = 0$ (subscript s) to $\varepsilon = 0.1$ (subscript e). Here $M = 0.5$, $Z = 2 + \mathrm{i}$ and $\omega = 30$. Contour plots are of $|p(r, \theta)|$, with contours at 0.05, 0.1, 0.2, 0.3, 0.4, 0.7 and 0.9 of the maximum magnitude.

$m = 2$ behaves in a similar way to that of figure 14 for no flow. However, the upstream-propagating trapped mode originates as a surface mode for $m = 0$ and travels significantly across the k-plane as it transitions from a surface mode ($\varepsilon = 0$, $\mathrm{Im}(k) \approx -16$) to a trapped mode and finally to an acoustic mode ($\varepsilon = 0.1$, $|\mathrm{Im}(k)| < 0.6$). This asymmetry is also shown in the mode shapes: figure 15*b* shows the downstream-propagating trapped mode for $\varepsilon = 0.05$ as reasonably broad but still noticeably dominant near the rigid splices; however, figure 15*f* shows that for the same value of $\varepsilon = 0.05$ the upstream-propagating trapped mode is already an acoustic mode and fills the duct, while for $\varepsilon = 0.005$ (shown in figure 15*d*) it is tightly trapped about the rigid splices. Figures 15*c*–*f* show the transition of this mode from surface mode to trapped mode to acoustic mode as ε is increased.

7. Conclusion

This paper gives an analytic solution for the pressure modes (solutions proportional to $\exp\{\mathrm{i}kx - \mathrm{i}\omega t\}$) of a cylindrical duct with lined walls apart from two symmetrically placed rigid splices of angular extent $\pm\varepsilon$ radians, with sheared axial flow; this generalizes previous analytic work to account for sheared axial flow and corrects the mistake in the boundary conditions of Campos & Oliveira (2004) mentioned in the introduction. In addition to the mathematical interest, this solution may prove useful as a reference solutions for validating numerical simulations. The solution is given as a Fourier sum (3.11,3.14) over solutions of the Pridmore–Brown equation (3.6), with a recurrence relation relating the coefficients of the sum (3.13,3.15). This expansion is derived using a Green's function method that not only correctly mimics the physics but also leaves no question over the completeness of the modes used in the expansion, as there might have been for a multimodal method using lined-duct modes as basis functions. A numerical procedure is given in §5 for solving the recurrence relation that has proved successful in all cases considered here. The assumption of two symmetrically placed rigid splices to an otherwise uniformly lined cylinder was chosen both for simplicity and for its practical relevance, although the authors foresee little difficulty in applying a similar procedure to different geometry, including differently placed splices, azimuthally variable liner impedances, or annular or rectangular cross-section ducts.

Treating the eigenvalue of the problem as the axial wavenumber k, §4 derived the second-order-accurate correction to k for small ε (4.2,4.9) and the first-order-accurate Fourier mode amplitudes (4.8); a similar result should be obtainable if the frequency ω is considered the eigenvalue. An interesting conclusion from the asymptotics made in §4.3 is that, for thin splices of width 2ε, the effect of the splices on modes which have a pressure antinode on the splice is $O(\varepsilon)$ while the effect of the splice on modes which have a pressure node on the splice is $O(\varepsilon^3)$. The accuracy of these asymptotics is verified in figure 3. These figures also show that $\varepsilon < 10^{-2}$ (approximately 0.6% unlined area or less) is necessary in some instances for the asymptotics to be accurate. However, the asymptotics may well still be useful for larger values of ε; figures 9, 10, 11 and 13 show that the level of agreement between the asymptotic and exact solutions for $\varepsilon = 0.1$ (approximately 6% unlined area) may be quantitatively reasonable (figures 9 and 13*b*), qualitatively indicative (figures 10 and 13*a*) or poor (figure 11). For the parameters considered here, it would seem that the asymptotics are generally more accurate for downstream-propagating than upstream-propagating modes, and more accurate for acoustic modes than for surface modes or trapped modes. The inaccuracy of the asymptotics in some cases is of practical importance, since it demonstrates that the effect of a splice of width 2ε can be larger than the expected $O(\varepsilon)$ even for moderately small values of ε, and therefore that even moderately small splices may play a more prominent

role than might have at first been expected. Moreover, the asymptotics provide a useful check on the accuracy of numerical solutions for very small splice widths which are hard to correctly resolve numerically.

The numerical procedure described in §5 for solving the recurrence relation compares favourably with other numerical solutions. The infinite azimuthal Fourier sum that is numerically truncated at N modes is shown in §5.2 to lead to an eigenvalue error that decays exponentially for increasing N. The comparable numerical scheme of Bi (2008) involves a doubly infinite sum of radial and azimuthal modes, which, if both are truncated at the same limit $N^{1/2}$ (as suggested by Bi for azimuthally nonuniform ducts) leads to N terms in the truncated sum and eigenvalue errors that decay at the rate $O(N^{5/2})$ (see Bi 2008, figure 3). The finite-element calculation of duct modes performed by Wright (2006) was reported to have taken approximately 19 minutes. On a similar computer, the same calculation using the method presented here would have taken approximately 1 minute, while if the splice widths were small enough that the asymptotics described here could be used the same calculation on a similar computer would have taken approximately 5 seconds. It should be noted, however, that the finite-element calculation of Wright (2006) could be adapted to irregular (i.e. non-circular and non-rectangular) cross-section ducts more easily than the method presented here.

A number of results are presented in §6 for the parameters $\omega = 31$, $m = 24$, $Z = 2 + \mathrm{i}$ and a peak Mach number of 0.5, these parameters being taken as typical for parameters of interest for an aeroengine intake (although note that when considering trapped modes in §6.5 we use $\omega = 30$ and $m \in \{0, 2\}$ in line with Bi *et al.* (2009)). For these parameters, the splice seems to have a most significant effect on modes close to cut-on cut-off transition. An interesting result is to note that the presence of a splice does not necessarily cause a decrease in damping, despite the reduction in lined surface; for example, figure 8*b* shows the upstream-propagating first-radial-order mode k_- to be more strongly damped with a splice than without, provided the splice is sufficiently thin. The splice may also cause significant scattering into other azimuthal-order modes; for example, figure 10*b* shows that the first-radial-order upstream-propagating mode k_-, which for $\varepsilon = 0$ was of 24th azimuthal order, has, through increasing ε smoothly from 0 to 0.1, obtained a dominating 8th azimuthal order term and substantial 16th and 20th order terms. The effect of this can clearly be seen in figure 6, and is also captured qualitatively in the asymptotic results shown in figure 10*b*. Overall, very roughly, the effect of a thin splice on the axial wavenumber k compared with an unspliced duct is seen from figure 12 to be of comparable order of magnitude to the effect of a thin shear layer over the lining compared with a uniform mean flow; this suggests that the inaccuracy caused by using a uniform mean flow and the Myers (1980) boundary condition (Brambley 2011*b*; Rienstra & Darau 2011; Joubert 2010) is comparable to the inaccuracy of ignoring the effect of liner splices on modal propagation (although not necessarily on modal scattering by the ends of the lined section, which has not been considered here).

The case considered here is of an infinite length of lined spliced duct. A better approximation to real aeroengines would be to consider a finite length liner in an infinitely long rigid duct, as used in several mathematical, numerical and experimental studies (e.g. references in the introduction; Watson, Nark & Jones 2008). In addition to the different propagation characteristics within the lined spliced section, scattering at the two sudden axial discontinuities in boundary condition between rigid-walled and lined leads to further effects that are predicted to reduce the effectiveness of the lined section in absorbing sound in some instances (see the preceding references). While these end effects are not present in the model presented in this paper, they could be added by using a mode-matching condition at the two axial wall discontinuities; indeed, this is exactly

what was done by Wright (2006) and Gabard & Astley (2008), except that in these studies the duct eigenmodes were determined numerically within the lined spliced section using a two-dimensional finite-element method in place of the mathematical method presented here. The sudden discontinuities could also be incorporated using a Wiener–Hopf method (as in Koch & Möhring 1983; Rienstra 2007); moreover, such a method might also be used to extend the analytical infinite-duct solution given here to a semi-infinite duct and hence predict the radiation to the far field (as in, e.g. Munt 1977; Veitch & Peake 2008).

So far, the only modal solutions to the recurrence relations (3.13,3.15) found are solutions that have an equivalent $\varepsilon = 0$ mode. That this should always be so is not evidently true; for example, moving smoothly from a rigid-walled duct with $1/Z = 0$ to a lined duct with $1/Z \neq 0$ not only perturbs the $1/Z = 0$ modes, but also supports up to four extra surface modes with no rigid-wall equivalent (Rienstra 2003; Brambley & Peake 2006). It might have been thought that the trapped modes localized within the immediate neighbourhood of a splice might have had no unspliced equivalent, but in fact, as found by Bi *et al.* (2009) for no flow and here with flow, these trapped modes originate as unspliced surface wave modes of the appropriate azimuthal order (in this case, $m = 0$ and $m = 2$). At present, therefore, the existence of modes with no unspliced equivalent cannot be ruled out.

The support of E.J.B. by a Research Fellowship from Gonville & Caius College, Cambridge, is gratefully acknowledged.

REFERENCES

Abramowitz, M. & Stegun, I. A. 1964 *Handbook of Mathematical Functions*, 9th edn. Dover.

Alonso, J. S. & Burdisso, R. A. 2007 Green's functions for the acoustic field in lined ducts with uniform flow. *AIAA J.* **45** (11), 2677–2687.

Amos, D. E. 1986 Algorithm 644: A portable package for Bessel functions of a complex argument and nonnegative order. *ACM Transactions on Mathematical Software* **12**, 265–273.

Anderson, E., Bai, Z., Bischof, C., Blackford, S., Demmel, J., Dongarra, J., Du Croz, J., Greenbaum, A., Hammarling, S., McKenney, A. & Sorensen, D. 1999 *LAPACK Users' Guide*. Society for Industrial and Applied Mathematics.

Aurégan, Y., Starobinski, R. & Pagneux, V. 2001 Influence of grazing flow and dissipation effects on the acoustic boundary conditions at a lined wall. *J. Acoust. Soc. Am.* **109**, 59–64.

Bi, W. 2008 Calculations of modes in circumferentially nonuniform lined ducts. *J. Acoust. Soc. Am.* **123**, 2603–2612.

Bi, W. P., Pagneux, V., Lafarge, D. & Aurégan, Y. 2006 Modelling of sound propagationin a non-uniform lined duct using a multi-modal propagation method. *J. Sound Vib.* **289**, 1091–1111.

Bi, W. P., Pagneux, V., Lafarge, D. & Aurégan, Y. 2007 Characteristics of penalty mode scattering by rigid splices in lined ducts. *J. Acoust. Soc. Am.* **121** (3), 1303–1312.

Bi, W. P., Pagneux, V., Lafarge, D. & Aurégan, Y. 2009 Trapped modes at acoustically rigid splices. AIAA paper 2009-3105.

Brambley, E. J. 2009 Fundamental problems with the model of uniform flow over acoustic linings. *J. Sound Vib.* **322**, 1026–1037.

Brambley, E. J. 2011*a* Acoustic implications of a thin viscous boundary layer over a compliant surface or permeable liner. *J. Fluid Mech.* **678**, 348–378.

Brambley, E. J. 2011*b* A well-posed boundary condition for acoustic liners in straight ducts with flow. *AIAA J.* **49** (6), 1272–1282.

Brambley, E. J. & Peake, N. 2006 Classification of aeroacoustically relevant surface modes in cylindrical lined ducts. *Wave Motion* **43**, 301–310.

Campos, L. M. B. C. & Oliveira, J. M. G. S. 2004 On the acoustic modes in a cylindrical duct with an arbitrary wall impedance distribution. *J. Acoust. Soc. Am.* **116** (6), 3336–3347.

Cargill, A. M. 1993 Scattering from joins between liners in intake ducts with application to BR710 buzz-saw noise. *Tech. Rep.* TSG0688. Rolls–Royce.

Davis, A. M. J. & Llewellyn Smith, S. G. 2007 Perturbation of eigenvalues due to gaps in 2-d boundaries. *Proc. R. Soc. Lond.* A **463**, 759–786.

Duta, M. C. & Giles, M. B. 2006 A three-dimensional hybrid finite element/spectral analyis of noise radiation from turbofan inlets. *J. Sound Vib.* **296**, 623–642.

Eversman, W. & Beckemeyer, R. J. 1972 Transmission of sound in ducts with thin shear layers — Convergence to the uniform flow case. *J. Acoust. Soc. Am.* **52**, 216–220.

Fuller, C. R. 1984 Propagation and radiation of sound from flanged circular ducts with circumferentially varying wall admittances, I: Semi-infinite ducts. *J. Sound Vib.* **93**, 321–340.

Gabard, G. & Astley, R. J. 2008 A computational mode-matching approach for sound propagation in three-dimensional ducts with flow. *J. Sound Vib.* **315**, 1103–1124.

Joubert, L. 2010 Asymptotic approach for the mathematical and numerical analysis of the acoustic propagation in a strong shear flow. PhD thesis, École Polytechnique, (in French).

Koch, W. & Möhring, W. 1983 Eigensolutions for liners in uniform mean flow ducts. *AIAA J.* **21** (2), 200–213.

LeBlond, P. H. & Mysak, L. A. 1978 *Waves in the Ocean*. Elsevier.

Lighthill, M. J. 1978 *Waves in Fluids*. Cambridge.

McAlpine, A. & Wright, M. C. M. 2006 Acoustic scattering by a spliced turbofan inlet duct liner at supersonic fan speeds. *J. Sound Vib.* **292**, 911–934.

Munt, R. M. 1977 The interaction of sound with a subsonic jet issuing from a semi-infinite cylindrical pipe. *J. Fluid Mech.* **83**, 609–640.

Myers, M. K. 1980 On the acoustic boundary condition in the presence of flow. *J. Sound Vib.* **71**, 429–434.

Osipov, A. V. & Norris, A. N. 1999 The malyuzhinets thoery for scattering from wedge boundaries: A review. *Wave Motion* **29**, 313–340.

Pagneux, V., Amir, N. & Kergomard, J. 1996 A study of wave propagation in varying cross-section waveguides by modal decomposition. Part I. Theory and validation. *J. Acoust. Soc. Am.* **100**, 2034–2048.

Pridmore-Brown, D. C. 1958 Sound propagation in a fluid flowing through an attenuating duct. *J. Fluid Mech.* **4**, 393–406.

Rademaker, E. R., Sarin, S. L. & Parente, C. A. 1996 Experimental investigation on the influence of liner non-uniformities on prevailing modes. AIAA paper 96-1682.

Regan, B. & Eaton, J. 1999 Modelling the influence of acoustic liner non-uniformities on duct modes. *J. Sound Vib.* **219**, 859–879.

Rienstra, S. W. 2003 A classification of duct modes based on surface waves. *Wave Motion* **37**, 119–135.

Rienstra, S. W. 2007 Acoustic scattering at a hard–soft lining transition in a flow duct. *J. Engng Mathso* **59**, 451–475.

Rienstra, S. W. & Darau, M. 2011 Boundary-layer thickness effects of the hydrodynamic instability along an impednace wall. *J. Fluid Mech.* **671**, 559–573.

Rienstra, S. W. & Vilenski, G. G. 2008 Spatial instability of boundary layer along impedance wall. AIAA paper 2008-2932.

Sarin, S. L. & Rademaker, E. R. 1993 In-flight acoustic mode measurements in the turbofan engine inlet of fokker 100 aircraft. AIAA paper 93-4414.

Swinbanks, M. A. 1975 The sound field generated by a source distribution in a long duct carrying sheared flow. *J. Sound Vib.* **40**, 51–76.

Tam, C. K. W. & Ju, H. 2009 Finite difference computation of acoustic scattering by small surface inhomogeneities and discontinuities. *J. Comput. Phys.* **228**, 5917–5932.

Tam, C. K. W., Ju, H. & Chien, E. W. 2008 Scattering of acoustic duct modes by axial liner splices. *J. Sound Vib.* **310**, 1014–1035.

Tester, B. J. 1973 Some aspects of "sound" attenuation in lined ducts containing inviscid mean flows with boundary layers. *J. Sound Vib.* **28**, 217–245.

Tester, B. J. & de Mercato, L. 2006 Far-field directivity of rotor-alone tones radiated from fan intakes with spliced liners for different intake shapes, with flow. AIAA paper 2006-2456.

Tester, B. J., Powles, C. J., Baker, N. J. & Kempton, A. J. 2006 Scattering of sound by liner splices: A Kirchhoff model with numerical validation. *AIAA J.* **44** (9), 2009–2017.

Veitch, B. & Peake, N. 2008 Acoustic propagation and scattering in the exhaust flow from coaxial cylinders. *J. Fluid Mech.* **613**, 275–307.

Vilenski, G. G. & Rienstra, S. W. 2007 On hydrodynamic and acoustic modes in a ducted shear flow with wall lining. *J. Fluid Mech.* **583**, 45–70.

Watson, W. R. 1981 Noise suppression characteristics of peripherally segmented duct liners. *Tech. Rep.* TP-1904. NASA.

Watson, W. R., Nark, D. M. & Jones, M. G. 2008 Assessment of 3D codes for predicting liner attenuation in flow ducts. AIAA paper 2008-2828.

Wright, M. C. M. 2006 Hybrid analytical/numerical method for mode scattering in azimuthally non-uniform ducts. *J. Sound Vib.* **2006**, 583–594.

Yang, B. & Wang, T. Q. 2008 Investigation of the influence of liner hard-splices on duct radiation/propagation and mode scattering. *J. Sound Vib.* **315**, 1016–1034.